

A residual-based variational multiscale method with weak imposition of boundary conditions for buoyancy-driven flows

Songzhe Xu^a, Boshun Gao^a, Ming-Chen Hsu^a, Baskar Ganapathysubramanian^{a,*}

^a*Department of Mechanical Engineering, Iowa State University, 2025 Black Engineering, Ames, IA 50011, USA*

Abstract

There is growing interest in high fidelity simulations of buoyancy-driven flows in indoor environments. This is driven to a large extent by the push to utilize naturally occurring flows to reduce energy consumption in the built environment. Naturally occurring (buoyancy-driven) flows exhibit spatiotemporal thermal fluctuations, and accurately capturing these thermal variations is essential to calculate energy usage. In this work, we deploy a residual-based variational multiscale (VMS) finite element large-eddy simulation model for accurately modeling buoyancy-driven flows in enclosed environments. We use the canonical example of the Rayleigh–Bénard convection problem in 2D and 3D to verify and validate the VMS model. We show good comparison with benchmark numerical and experimental results across seven orders of magnitude variation in Rayleigh numbers ($Ra \sim 10^3$ to 10^{10}), covering laminar, transition, and turbulent regimes without any extra treatments. We additionally employ weak enforcement of Dirichlet boundary conditions for both velocity and temperature, and show that comparable results can be produced with much coarser meshes. This confirms that the VMS framework with weak imposition of Dirichlet boundary conditions is a computationally efficient approach to model buoyancy-driven flow physics in complex indoor environments.

Keywords: Residual-based variational multiscale; Weak imposition of boundary conditions; Buoyancy-driven convection; Large-eddy simulation

Contents

1	Introduction	2
2	Variational multiscale formulation and discretization	4
2.1	Strong and weak formulations of the continuous problem	4
2.2	Semi-discrete variational multiscale formulation	6

*Corresponding author
Email addresses: jmchsu@iastate.edu (Ming-Chen Hsu), baskarg@iastate.edu (Baskar Ganapathysubramanian)

2.3	Weakly imposed boundary conditions for both velocity and temperature	8
3	Numerical method and implementation	9
3.1	Time discretization and averaging over time	9
3.2	Block iterative method	10
3.3	Non-dimensional form	10
3.4	Implementation	11
4	Rayleigh–Bénard convection problem	12
4.1	2D cases	13
4.1.1	Mesh convergence studies	13
4.1.2	Comparisons of averaged Nusselt numbers and maximum velocities	13
4.1.3	Comparisons of mean profiles	15
4.2	3D cases	16
4.2.1	Mesh convergence studies	16
4.2.2	Comparisons of averaged Nusselt numbers	18
4.2.3	Comparisons of mean profiles	18
4.2.4	Comparisons of fluctuation profiles for the turbulent case	21
4.3	2D cases with weakly imposed boundary conditions	22
4.3.1	Mesh convergence studies	22
4.3.2	Comparisons with strong BC for the turbulent case	23
4.4	3D case with weakly imposed boundary conditions	25
4.4.1	Mesh convergence studies	25
4.4.2	Comparisons with strong BC results	25
5	Conclusions	27

1. Introduction

Accurate simulation of coupled heat and momentum transport in incompressible fluids is essential in a variety of engineering applications. One critical application is in building simulations, which involves understanding and controlling the thermal and flow physics in complex, enclosed domains. There has been increasing interest in understanding and engineering the coupled thermal and momentum transport in inhabited domains so as to simultaneously increase the efficiency with which buildings use energy, while maintaining indoor comfort. Lower energy consumption reduces the impact of buildings on human health and the environment, reduces greenhouse gas emissions, enables the integration of onsite renewables, and lowers the economic hurdles to home ownership. According to the U.S. Energy Information Administration (EIA), even incremental improvements

in energy efficiency have a significant impact on the U.S. energy budget, since buildings are responsible for approximately 40% of the total U.S. energy consumption [1].

One promising approach towards enhancing the energy sustainability of buildings has been to integrate passive natural ventilation (or buoyancy-driven flows) into the building environmental control system [2–7]. Such an approach requires a detailed understanding of how buoyancy-driven flows affect, and are affected by, different thermal boundary conditions. This is an area where robust and reliable computational tools have been scarce, especially for the building design community [8].

Standard computational fluid dynamics (CFD) approaches based on Reynolds-averaged Navier–Stokes (RANS) models have been shown not to work well for this class of problems [9–14]¹ and require site-specific and application-specific models [15]. In particular, most RANS-based models are unable to reliably predict boundary heat transfer coefficients (or Nusselt numbers) across the necessarily large range of Rayleigh numbers (Ra) that occur during building operation. In even comparatively simple geometries, the variation in thermal boundary conditions can result in Rayleigh numbers spanning from 10^3 (laminar) to 10^{10} (turbulent), thus making it necessary for any methods used to reliably and automatically predict Nusselt numbers across this range of flow conditions.

Recent results suggest that a more high-fidelity approach using large-eddy simulation (LES) would enable accurately accounting for the effects of natural ventilation [16–18]. Large-eddy simulation based approaches have been applied for buoyancy-driven flows [19–22] with success. This is particularly promising with the increase in availability of (as well as ease of access, and use of) high-performance computing resources that make such simulations possible. Motivated by the need to reliably model thermal transport in complex enclosed domains, we deploy a finite element LES model based on the variational multiscale (VMS) method [23–25] for buoyancy-driven flows. The formulation is similar to the semi-discrete version of the space–time VMS (ST–VMS) method for the incompressible flows with thermal coupling proposed by Takizawa et al. [26]. The VMS approach uses variational projections in place of the traditional filtered equations in LES and focuses on modeling the fine-scale equations. The method is derived completely from the incompressible Navier–Stokes and heat equations and does not employ any eddy viscosity.

Such VMS formulations have shown significant success in modeling isothermal turbulent flows [25, 27], and have been extended to a wide range of engineering applications. Yan et al. [28] proposed a closure model for the fine scales of VMS formulations in density-stratified flows.

¹This is often the case due to rapid variations in thermal boundary conditions caused by fluctuations in wind loads, as well as variations in incident solar radiation. Additionally, indoor spaces exhibit localized regions of laminar, transition and turbulent behavior. RANS based approaches have difficulty tracking this without *a priori* information, which is usually not available.

Bazilevs et al. [29] proposed a VMS formulation in an ALE framework (ALE–VMS) for stratified flows on moving domains. Takizawa et al. [26] developed the ST–VMS formulation for a thermo-fluid analysis of a ground vehicle and its tires. Related work of ALE–VMS and ST–VMS in complex systems can also be found in references [30–34]. Successful extensions of VMS formulations in other fields have also been carried out, such as multiphase flows [35], magnetohydrodynamic (MHD) flows [36], and compressible flows [37].

In this work, the VMS formulation for buoyancy-driven flows is augmented with weakly enforced Dirichlet boundary conditions. The weak enforcement of Dirichlet boundary conditions in fluid mechanics, first proposed by Bazilevs and Hughes [38], improves the accuracy of simulations of flows with thin boundary layers. Such a strategy releases the point-wise no-slip condition imposed at the boundary of the fluid domain and instead allows the flow to slip on the solid surface, thus minimizing the mesh resolution required to track the steep gradients close to the boundaries. Note that this effect reliably imitates the presence (and effect) of the thin boundary layer [39, 40]. Enforcing Dirichlet boundary conditions weakly allows for an accurate overall flow solution even if the mesh size in the wall-normal direction is relatively large. This approach has substantially benefited efficient simulations of turbulent flow scenarios as demonstrated in Bazilevs et al. [39, 41]. It has since been successfully extended to applications of incompressible thermal flows such as vehicle disk break simulations and wind turbine simulations [29, 42, 43]. The weak enforcement of Dirichlet boundary conditions is of particular interest in this work due to the thin boundary layers present in the built environment.

This paper is outlined as follows. In Section 2, we develop the formulations of VMS method and the weak imposition of Dirichlet boundary conditions for both velocity and temperature. Section 3 illustrates the numerical implementation of the proposed method. Section 4 verifies and validates the VMS formulation and shows its ability to produce accurate results for an extensive range of Ra from 10^3 to 10^{10} for both 2D and 3D cases. The advantage of applying weakly enforced Dirichlet boundary conditions is also demonstrated in this section. Section 5 draws conclusions and outlines the potential of applying the proposed method in the future work of indoor simulations for complex buildings.

2. Variational multiscale formulation and discretization

2.1. Strong and weak formulations of the continuous problem

In what follows, $\Omega \subset \mathbb{R}^d$, $d = 2, 3$, denotes the spatial domain of the problem with boundary Γ . The Navier–Stokes equations of incompressible flow may be written on Ω as

$$\frac{\partial \mathbf{u}}{\partial t} + \nabla \cdot (\mathbf{u} \otimes \mathbf{u}) = -\frac{1}{\rho} \nabla p + \nu \nabla^2 \mathbf{u} + \mathbf{f}(\mathbf{u}, T), \quad (1)$$

$$\nabla \cdot \mathbf{u} = 0, \quad (2)$$

where \mathbf{u} is the velocity, \mathbf{f} is the forcing function (velocity–temperature coupling), p is the pressure, ρ is the fluid density, ν is the kinetic viscosity, T is the temperature, and ∇ is the spatial gradients. The energy equation may be written on Ω as

$$\frac{\partial T}{\partial t} + \nabla \cdot (\mathbf{u}T) = \alpha \nabla^2 T, \quad (3)$$

where α is the thermal diffusivity. Based on our application scenario, we assume the Boussinesq approximation for the velocity–temperature coupling, thus

$$\mathbf{f} = -\hat{\mathbf{g}}\beta(T - T_r), \quad (4)$$

where $\hat{\mathbf{g}}$ is the gravitational acceleration, β is the thermal expansion, and T_r is the reference temperature. The problem (1)–(4) is subject to suitable boundary conditions, defined on the domain boundary, $\Gamma = \Gamma^D \cup \Gamma^N$ with $\Gamma^D = \Gamma_{\mathbf{u}}^D \cup \Gamma_T^D$ and $\Gamma^N = \Gamma_{\mathbf{u}}^N \cup \Gamma_T^N$:

$$\mathbf{u} = \mathbf{u}_g \quad \text{on } \Gamma_{\mathbf{u}}^D, \quad (5)$$

$$T = T_g \quad \text{on } \Gamma_T^D, \quad (6)$$

$$-\frac{p}{\rho} \mathbf{n} + \nu \nabla \mathbf{u} \cdot \mathbf{n} = \mathbf{h}_{\mathbf{u}} \quad \text{on } \Gamma_{\mathbf{u}}^N, \quad (7)$$

$$\alpha \nabla T \cdot \mathbf{n} = h_T \quad \text{on } \Gamma_T^N, \quad (8)$$

where \mathbf{u}_g and T_g are prescribed velocity and temperature at the Dirichlet boundaries $\Gamma_{\mathbf{u}}^D$ and Γ_T^D , respectively, $\mathbf{h}_{\mathbf{u}}$ and h_T are given functions at the Neumann boundaries $\Gamma_{\mathbf{u}}^N$ and Γ_T^N , respectively, and \mathbf{n} is the unit normal vector.

Let \mathcal{V} be the space of both trial solutions and test functions. The variational formulation is stated as: Find $\{\mathbf{u}, p, T\} \in \mathcal{V}$ such that $\forall \{\mathbf{w}, q, l\} \in \mathcal{V}$,

$$B(\{\mathbf{w}, q, l\}, \{\mathbf{u}, p, T\}) - F(\{\mathbf{w}, q, l\}, \{\mathbf{u}, p, T\}) = 0, \quad (9)$$

where

$$\begin{aligned} B(\{\mathbf{w}, q, l\}, \{\mathbf{u}, p, T\}) &= \int_{\Omega} \mathbf{w} \cdot \frac{\partial \mathbf{u}}{\partial t} \, d\Omega - \int_{\Omega} \nabla \mathbf{w} : (\mathbf{u} \otimes \mathbf{u}) \, d\Omega + \int_{\Omega} \nabla \mathbf{w} : \nu \nabla \mathbf{u} \, d\Omega \\ &\quad - \int_{\Omega} \frac{p}{\rho} \nabla \cdot \mathbf{w} \, d\Omega + \int_{\Omega} q \nabla \cdot \mathbf{u} \\ &\quad + \int_{\Omega} l \frac{\partial T}{\partial t} \, d\Omega - \int_{\Omega} \nabla l \cdot (\mathbf{u}T) + \int_{\Omega} \nabla l \cdot \alpha \nabla T \, d\Omega, \end{aligned} \quad (10)$$

and

$$\begin{aligned}
F(\{\mathbf{w}, q, l\}, \{\mathbf{u}, p, T\}) &= \int_{\Omega} \mathbf{w} \cdot \mathbf{f} \, d\Omega - \int_{\Gamma_{\mathbf{u}}^N} (\mathbf{w} \cdot \mathbf{u}) \mathbf{u} \cdot \mathbf{n} \, d\Gamma + \int_{\Gamma_{\mathbf{u}}^N} \mathbf{w} \cdot \mathbf{h}_{\mathbf{u}} \, d\Gamma \\
&\quad - \int_{\Gamma_T^N} l T \mathbf{u} \cdot \mathbf{n} \, d\Gamma + \int_{\Gamma_T^N} l h_T \, d\Gamma.
\end{aligned} \tag{11}$$

Note that \mathbf{f} is a function of T .

2.2. Semi-discrete variational multiscale formulation

Following the development in Takizawa et al. [26] and extending the variational multiscale theory [25] to the buoyancy-driven convection problem, the space of trial solution and weighting function is split into coarse and fine scales as $\mathcal{V} = \mathcal{V}^h \oplus \mathcal{V}'$, where the superscript h denotes resolved coarse scales represented by the finite element discretization and the primed quantity corresponds to the unresolved fine scales that need to be modeled. The decomposition of the space leads to

$$\{\mathbf{u}, p, T\} = \{\mathbf{u}^h, p^h, T^h\} + \{\mathbf{u}', p', T'\}, \tag{12}$$

$$\{\mathbf{w}, q, l\} = \{\mathbf{w}^h, q^h, l^h\} + \{\mathbf{w}', q', l'\}. \tag{13}$$

Substituting Eq. (12) into Eq. (9) and choosing $\{\mathbf{w}, q, l\} = \{\mathbf{w}^h, q^h, l^h\}$ yields

$$B(\{\mathbf{w}^h, q^h, l^h\}, \{\mathbf{u}^h, p^h, T^h\} + \{\mathbf{u}', p', T'\}) - F(\{\mathbf{w}^h, q^h, l^h\}, \{\mathbf{u}^h, p^h, T^h\} + \{\mathbf{u}', p', T'\}) = 0. \tag{14}$$

Because $\{\mathbf{w}^h, q^h, l^h\}$ are in a finite-dimensional space, Eq. (14) leads to a finite-dimensional system of equations for which the coarse scale variables $\{\mathbf{u}^h, p^h, T^h\}$ are the unknowns. The variational statement (14) indicates that the coarse scale equations depend on the fine-scale fields. The fine scales $\{\mathbf{u}', p', T'\}$ are not given and their effects on the coarse-scale equations must, therefore, be modeled. To simplify Eq. (14), three assumptions are typically employed: (1) the fine scales are orthogonal to the coarse scales with respect to the inner-product generated by the viscous term; (2) the fine scales are quasi-static; and (3) the fine scales variables are zero at the domain boundary.

We decompose the domain Ω into a collection of N_{el} disjoint elements each denoted by Ω^e , $\Omega = \bigcup_{e=1}^{N_{\text{el}}} \Omega^e$. We follow the developments in Bazilevs et al. [25] and arrive at the semi-discrete variational multiscale formulation for the buoyancy-driven convection problem as: Find $\{\mathbf{u}^h, p^h, T^h\} \in \mathcal{V}^h$ such that $\forall \{\mathbf{w}^h, q^h, l^h\} \in \mathcal{V}^h$,

$$B^{\text{VMS}}(\{\mathbf{w}^h, q^h, l^h\}, \{\mathbf{u}^h, p^h, T^h\}) - F^{\text{VMS}}(\{\mathbf{w}^h, q^h, l^h\}, \{\mathbf{u}^h, p^h, T^h\}) = 0, \tag{15}$$

where

$$\begin{aligned}
& B^{\text{VMS}}(\{\mathbf{w}^h, q^h, l^h\}, \{\mathbf{u}^h, p^h, T^h\}) \\
&= \int_{\Omega} \mathbf{w}^h \cdot \frac{\partial \mathbf{u}^h}{\partial t} \, d\Omega + \int_{\Omega} \mathbf{w}^h \cdot (\mathbf{u}^h \cdot \nabla \mathbf{u}^h) \, d\Omega + \int_{\Omega} \nabla \mathbf{w}^h : \nu \nabla \mathbf{u}^h \, d\Omega \\
&- \int_{\Omega} \frac{p^h}{\rho} \nabla \cdot \mathbf{w}^h \, d\Omega + \int_{\Omega} q^h \nabla \cdot \mathbf{u}^h \\
&+ \int_{\Omega} l^h \frac{\partial T^h}{\partial t} \, d\Omega + \int_{\Omega} l^h (\mathbf{u}^h \cdot \nabla T^h) \, d\Omega + \int_{\Omega} \nabla l^h \cdot \alpha \nabla T^h \, d\Omega \\
&- \sum_{e=1}^{N_{\text{el}}} \int_{\Omega^e} (\mathbf{u}^h \cdot \nabla \mathbf{w}^h + \nabla q^h) \cdot \mathbf{u}' \, d\Omega - \sum_{e=1}^{N_{\text{el}}} \int_{\Omega^e} (\mathbf{u}^h \cdot \nabla l^h) T' \, d\Omega - \sum_{e=1}^{N_{\text{el}}} \int_{\Omega^e} \frac{p'}{\rho} \nabla \cdot \mathbf{w}^h \, d\Omega \\
&+ \sum_{e=1}^{N_{\text{el}}} \int_{\Omega^e} \mathbf{w}^h \cdot (\mathbf{u}' \cdot \nabla \mathbf{u}^h) \, d\Omega - \sum_{e=1}^{N_{\text{el}}} \int_{\Omega^e} \nabla \mathbf{w}^h : (\mathbf{u}' \otimes \mathbf{u}') \, d\Omega \\
&+ \sum_{e=1}^{N_{\text{el}}} \int_{\Omega^e} l^h (\mathbf{u}' \cdot \nabla T^h) \, d\Omega - \sum_{e=1}^{N_{\text{el}}} \int_{\Omega^e} \nabla l^h \cdot (\mathbf{u}' T') \, d\Omega, \tag{16}
\end{aligned}$$

and

$$\begin{aligned}
& F^{\text{VMS}}(\{\mathbf{w}^h, q^h, l^h\}, \{\mathbf{u}^h, p^h, T^h\}) \\
&= \int_{\Omega} \mathbf{w}^h \cdot \mathbf{f}^h \, d\Omega + \sum_{e=1}^{N_{\text{el}}} \int_{\Omega^e} \mathbf{w}^h \cdot \mathbf{f}' \, d\Omega + \int_{\Gamma_{\mathbf{u}}^N} \mathbf{w}^h \cdot \mathbf{h}_{\mathbf{u}} \, d\Gamma + \int_{\Gamma_T^N} l^h \mathbf{h}_T \, d\Gamma. \tag{17}
\end{aligned}$$

In the above, $\mathbf{f}' = -\hat{\mathbf{g}}\beta T'$. Bazilevs et al. [25] proposed solutions of the fine scale variables as a linear approximation based on the residuals of the coarse-scale equations for isothermal flows. Following the development in Takizawa et al. [26] and extending the same approximation to the energy equation, we have

$$\mathbf{u}' = -\tau_{\text{M}} \mathbf{r}_{\text{M}}(\{\mathbf{u}^h, p^h, T^h\}), \tag{18}$$

$$p' = -\tau_{\text{C}} r_{\text{C}}(\mathbf{u}^h), \tag{19}$$

$$T' = -\tau_{\text{E}} r_{\text{E}}(\{\mathbf{u}^h, T^h\}), \tag{20}$$

where

$$\mathbf{r}_{\text{M}} = \frac{\partial \mathbf{u}^h}{\partial t} + \mathbf{u}^h \cdot \nabla \mathbf{u}^h + \frac{1}{\rho} \nabla p^h - \nu \nabla^2 \mathbf{u}^h - \mathbf{f}^h, \tag{21}$$

$$r_{\text{C}} = \nabla \cdot \mathbf{u}^h, \tag{22}$$

$$r_{\text{E}} = \frac{\partial T^h}{\partial t} + \mathbf{u}^h \cdot \nabla T^h - \alpha \nabla^2 T^h, \tag{23}$$

$$\tau_M = \left(\frac{4}{\Delta t^2} + \mathbf{u}^h \cdot \mathbf{G} \mathbf{u}^h + C_M \nu^2 \mathbf{G} : \mathbf{G} \right)^{-1/2}, \quad (24)$$

$$\tau_C = (\tau_M \mathbf{g} \cdot \mathbf{g})^{-1}, \quad (25)$$

$$\tau_E = \left(\frac{4}{\Delta t^2} + \mathbf{u}^h \cdot \mathbf{G} \mathbf{u}^h + C_E \alpha^2 \mathbf{G} : \mathbf{G} \right)^{-1/2}, \quad (26)$$

and

$$G_{ij} = \frac{\partial \xi_k}{\partial x_i} \frac{\partial \xi_k}{\partial x_j}, \quad (27)$$

$$\mathbf{G} : \mathbf{G} = G_{ij} G_{ij}, \quad (28)$$

$$g_i = \sum_{j=1}^d \frac{\partial \xi_j}{\partial x_i}, \quad (29)$$

$$\mathbf{g} \cdot \mathbf{g} = g_i g_i. \quad (30)$$

In the above, C_M and C_E are positive constants that can be derived from element-wise inverse estimates [44, 45]. \mathbf{G} and \mathbf{g} are mesh-dependent quantities related to the mapping from physical elements to the isoparametric element. The repeated indices in Eq. (27)–(30) follow summation rule of index notation.

The terms in the second, third and fourth line in Eq. (16) make up the standard Galerkin form, $B(\{\mathbf{w}^h, q^h, l^h\}, \{\mathbf{u}^h, p^h, T^h\})$, of the Navier–Stokes equations and energy equation. Note, however, that we expand the coarse-scale convection terms in these equations into their convective form [46]. The fifth line incorporates the classical stabilization terms, such as streamline-upwind/Petrov–Galerkin (SUPG) and pressure-stabilizing/Petrov–Galerkin (PSPG) [47, 48]. We also have the SUPG stabilization term in the energy equation. The last two lines incorporate additional terms produced by the VMS formulation [25]. The terms incorporating the fine-scale variables added onto the standard Galerkin terms can be interpreted as the combination of the classical stabilization and VMS turbulence modeling for the buoyancy-driven convection problem.

2.3. Weakly imposed boundary conditions for both velocity and temperature

Weak imposition of Dirichlet boundary conditions in the sense of Nitsche’s method [49] has been successfully developed and applied to incompressible isothermal [27, 38–41, 50] and thermal [29, 42, 43] flows, compressible flows [51, 52], and immersogeometric flow analysis [53–57]. Building upon the previous work, we apply the weak imposition of Dirichlet boundary conditions to the two-equation system here. Decomposing the domain boundary Γ into N_{eb} surface elements each denoted by Γ^{b} , the semi-discrete formulation with weakly imposed boundary conditions for

the buoyancy-driven convection problem may be written as

$$\begin{aligned}
& B^{\text{VMS}}(\{\mathbf{w}^h, q^h, l^h\}, \{\mathbf{u}^h, p^h, T^h\}) - F^{\text{VMS}}(\{\mathbf{w}^h, q^h, l^h\}, \{\mathbf{u}^h, p^h, T^h\}) \\
& - \sum_{b=1}^{N_{\text{eb}}} \int_{\Gamma^b \cap \Gamma_{\mathbf{u}}^{\text{D}}} \mathbf{w}^h \cdot \left(-\frac{p^h}{\rho} \mathbf{n} + \nu \nabla \mathbf{u}^h \cdot \mathbf{n} \right) d\Gamma - \sum_{b=1}^{N_{\text{eb}}} \int_{\Gamma^b \cap \Gamma_T^{\text{D}}} l^h \alpha \nabla T^h \cdot \mathbf{n} d\Gamma \\
& - \sum_{b=1}^{N_{\text{eb}}} \int_{\Gamma^b \cap \Gamma_{\mathbf{u}}^{\text{D}}} \left(\nu \nabla \mathbf{w}^h \cdot \mathbf{n} + \frac{q^h}{\rho} \mathbf{n} \right) \cdot (\mathbf{u}^h - \mathbf{u}_g) d\Gamma - \sum_{b=1}^{N_{\text{eb}}} \int_{\Gamma^b \cap \Gamma_T^{\text{D}}} \alpha \nabla l^h \cdot \mathbf{n} (T^h - T_g) d\Gamma \\
& + \sum_{b=1}^{N_{\text{eb}}} \int_{\Gamma^b \cap \Gamma_{\mathbf{u}}^{\text{D}}} \tau_M^B \mathbf{w}^h \cdot (\mathbf{u}^h - \mathbf{u}_g) d\Gamma + \sum_{b=1}^{N_{\text{eb}}} \int_{\Gamma^b \cap \Gamma_T^{\text{D}}} \tau_E^B l^h (T^h - T_g) d\Gamma = 0. \tag{31}
\end{aligned}$$

The second line in Eq. (31) incorporates the consistency terms arising from the integration by parts when deriving the weak form of pressure, viscous, and heat diffusion terms in Eqs. (1)–(3) without setting the test functions to zero at the Dirichlet boundaries. These terms ensure the variational consistency of the method. Note that since the convective form for the coarse-scale convection terms is used, there are no boundary terms generated from them. The third line incorporates the so-called adjoint consistency terms, which are linked to optimal convergence of the discrete solution in lower-order norms [58]. The fourth line incorporates the penalty-like stabilization terms, with τ_M^B and τ_E^B being the stabilization parameters, that penalize the deviation of the discrete solution from its prescribed value at the boundary. Also, these terms are necessary to ensure the stability (or coercivity) of the discrete formulation, which may be lost due to the introduction of consistency and adjoint consistency terms [59, 60].

It has been noted in previous work that the stabilization parameters in weak boundary condition formulations cannot be too large. If they are too large, they assume a penalty-type character, affecting the conditioning of the stiffness matrix and overshadowing the variational consistency. The parameters should not be too small either due to stability considerations. Bazilevs and Hughes [38] proposed τ_M^B to have the following form $\tau_M^B = C_M^B \nu / h$, where h is the wall-normal element size and C_M^B is a positive constant that can be computed from an appropriate element-level inverse estimate [45]. Similarly, we define $\tau_E^B = C_E^B \alpha / h$, with C_E^B having the same definition as C_M^B .

3. Numerical method and implementation

3.1. Time discretization and averaging over time

We employ a finite difference based fully implicit backward Euler scheme for the discretization of the equations in time. The time step size Δt is selected using the CFL condition. We define the set of variables as $\mathbf{U} = \{\mathbf{u}^h, p^h, T^h\}$. The time-averaged statistics of $\bar{\mathbf{U}}$ in the quasi-steady state can be expressed as $\bar{\mathbf{U}} = \int_{t_s}^t \mathbf{U} dt / (t - t_s)$, where t_s is the time at which we start collecting data to

compute the averages, and $t-t_s$ is a sufficiently long time interval. The fluctuations of the variables are defined as $\mathbf{U}^F = \mathbf{U} - \bar{\mathbf{U}}$. We average the square of the velocity components, pressure, and temperature in \mathbf{U}^F in the same time interval to obtain the time-averaged statistics of the fluctuation quantities. We report the mean profiles $\bar{\mathbf{U}}$ and the fluctuation profiles in Section 4 to verify and validate our framework.

3.2. Block iterative method

We employ the Newton–Raphson method and a block-iterative strategy [61] to solve the set of nonlinear Navier–Stokes and energy equations (due to the very stiff nature of the fully-coupled system). In the block-iterative strategy, we form two individual systems, one for the Navier–Stokes equations and one for the energy equation, and solve them self-consistently at every time step. For each block iteration, we first solve the energy equation for the temperature field with velocity and pressure fields known from the previous iteration (or time step if in the first iteration). The newly obtained temperature field is passed to the Navier–Stokes equations to solve for the velocity and pressure fields. We then update every variable and compute the L_2 norm error of the fields. We continue the self-consistent block iterations until the relative L_2 norm error for every variable field is less than a tolerance.² The flowchart of the approach is shown in Figure 1.

3.3. Non-dimensional form

We solve the equations in their non-dimensional form. This is done by scaling the variables as follows:

$$\mathbf{x}^* = \frac{\mathbf{x}}{L_0}, \quad \mathbf{u}^* = \frac{\mathbf{u}}{u_0}, \quad t^* = \frac{t}{t_0}, \quad p^* = \frac{p}{\rho u_0^2}, \quad \theta = \frac{T - T_r}{\Delta T}. \quad (32)$$

Here, $(\cdot)^*$ represents dimensionless quantities, L_0 is the characteristic length of the problem, u_0 is the characteristic velocity, $u_0 = (\hat{g}\beta\Delta TL_0)^{1/2}$ for buoyancy-driven flows, where \hat{g} is the acceleration due to gravity, $t_0 = L_0/u_0$ is the characteristic time, $\Delta T = T_h - T_c$ is the temperature differential of the highest temperature T_h and the lowest temperature T_c , and θ is the dimensionless temperature. We choose the reference temperature T_r to be the lowest temperature T_c . The non-dimensionalization results in the following set of equations:

$$\frac{\partial \mathbf{u}^*}{\partial t^*} + \nabla^* \cdot (\mathbf{u}^* \otimes \mathbf{u}^*) + \nabla^* p^* - \sqrt{\frac{Pr}{Ra}} \nabla^{*2} \mathbf{u}^* - \mathbf{f}^* = 0 \quad (33)$$

$$\nabla^* \cdot \mathbf{u}^* = 0 \quad (34)$$

$$\frac{\partial \theta}{\partial t^*} + \nabla^* \cdot (\mathbf{u}^* \theta) - \sqrt{\frac{1}{PrRa}} \nabla^{*2} \theta = 0, \quad (35)$$

²In this work, we find a tolerance of 0.1% provides a good balance between the computational time and solution accuracy.

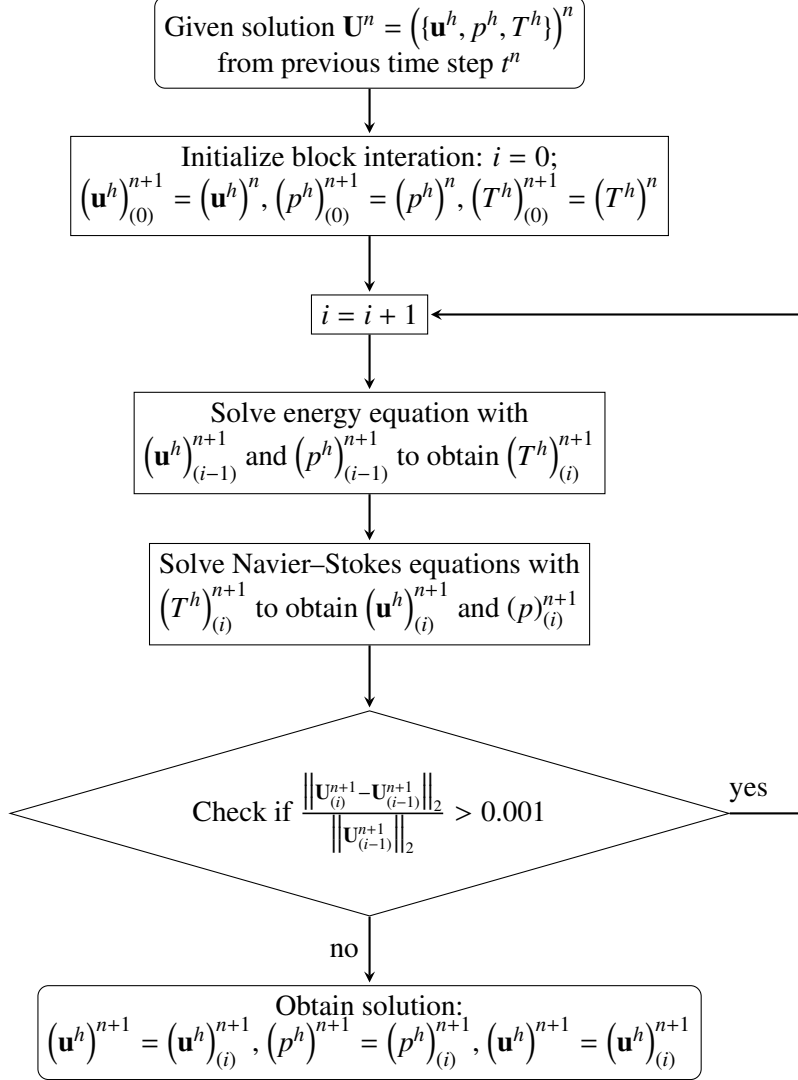


Figure 1: A flowchart of the block-iterative strategy for solving the Navier–Stokes and energy equations system.

where $Ra = \hat{g}\beta\Delta TL_0^3/\nu\alpha$ is the Rayleigh number, $Pr = \nu/\alpha$ is the Prandtl number, $\nabla^* = \frac{\partial}{\partial \mathbf{x}^*}$ is the dimensionless spacial gradient operator, and $\mathbf{f}^* = \mathbf{e}_{\hat{g}}\theta$, where $\mathbf{e}_{\hat{g}}$ is the unit vector pointing in the direction of gravity.

3.4. Implementation

We implement the variational multiscale method and the weakly imposed boundary condition method for buoyancy-driven flows within our in-house parallel finite element framework. We couple our framework with an open source package PETSc [62], to employ its scalable nonlinear equation solvers (SNES) as well as its linear Krylov subspace solvers (KSP). Domain decomposition is performed with the parallel partitioning package ParMETIS [63].

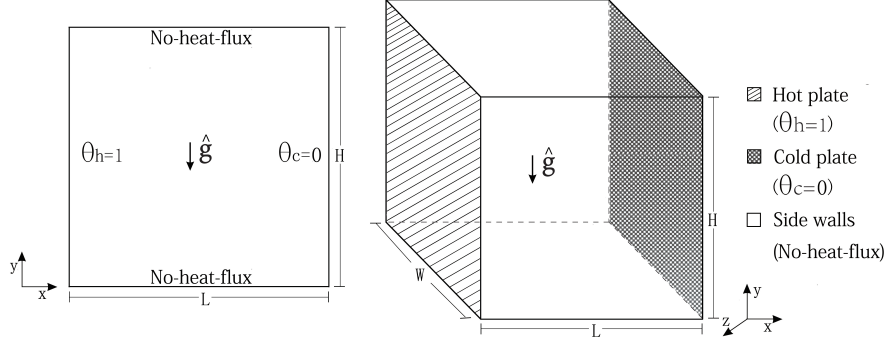


Figure 2: Geometries and boundary conditions for the 2D (left) and 3D (right) cases of the Rayleigh–Bénard convection problem.

4. Rayleigh–Bénard convection problem

The Rayleigh–Bénard convection phenomena serves as the canonical problem that we choose to model in this work. This is a very well studied problem, with extensive experimental and computational results available for comparison. It is also a typical representative of buoyancy-driven flows in enclosed geometries that is relevant to our application. We consider a (non-dimensional) Rayleigh–Bénard convection problem with temperature differential applied on the vertical walls. We consider simulations in both 2D and 3D cases as shown in Figure 2. No-slip boundary conditions are applied on all walls.

We first show 2D results with strongly imposed boundary conditions. Simulations are performed for an extensive range of Ra numbers from 10^3 to 10^{10} at $Pr = 0.7$. The surface (hot wall) averaged Nusselt number \overline{Nu} is examined for the mesh convergence studies. This is motivated from the building science application where the net heat transfer from surfaces (given by the Nusselt number) is a key quantity of interest. The local Nu and surface averaged \overline{Nu} on the hot wall Γ_H with area A_H are defined as $Nu = \nabla^* \theta \cdot \mathbf{n}$ and $\overline{Nu} = \int_{\Gamma_H} Nu d\Gamma / A_H$, respectively. We also present the convergence of mean temperature profile along horizontal median line for one laminar case ($Ra = 10^5$) and one turbulent case ($Ra = 10^9$) to show the element-wise convergence.

We then show 3D results with strongly imposed boundary conditions. Mesh convergence studies for a laminar case with $Ra = 1.89 \times 10^5$ and a turbulent case with $Ra = 1.5 \times 10^9$ are performed. The results of \overline{Nu} , mean profiles, and fluctuation profiles are compared with experimental data and numerical results from the literature.

Finally, the weak enforcement of Dirichlet boundary conditions for both velocity and temperature is applied for the 2D and 3D cases. Mesh convergence studies and comprehensive comparisons with results obtained using strongly imposed boundary conditions are carried out to illustrate the computational advantages of the weakly imposed boundary conditions.

Table 1: 2D mesh convergence results for \overline{Nu} . The underline indicates the mesh size at which the Nusselt number has reached a converged value (difference of \overline{Nu} for two successive mesh sizes is less than 2%).

Uniform mesh	Ra (Laminar)			Ra (Transition)		Ra (Turbulent)		
	10^3	10^4	10^5	10^6	10^7	10^8	10^9	10^{10}
50×50	<u>1.117</u>	<u>2.240</u>	<u>4.488</u>	8.585	14.99	22.78	28.90	33.15
100×100	1.118	2.244	4.511	<u>8.772</u>	<u>16.15</u>	27.91	43.23	57.66
200×200	1.118	2.245	4.516	8.810	16.44	<u>29.67</u>	51.18	81.22
400×400	-	-	-	-	-	30.1	<u>53.81</u>	93.40
600×600	-	-	-	-	-	-	54.29	<u>96.63</u>
800×800	-	-	-	-	-	-	-	97.29

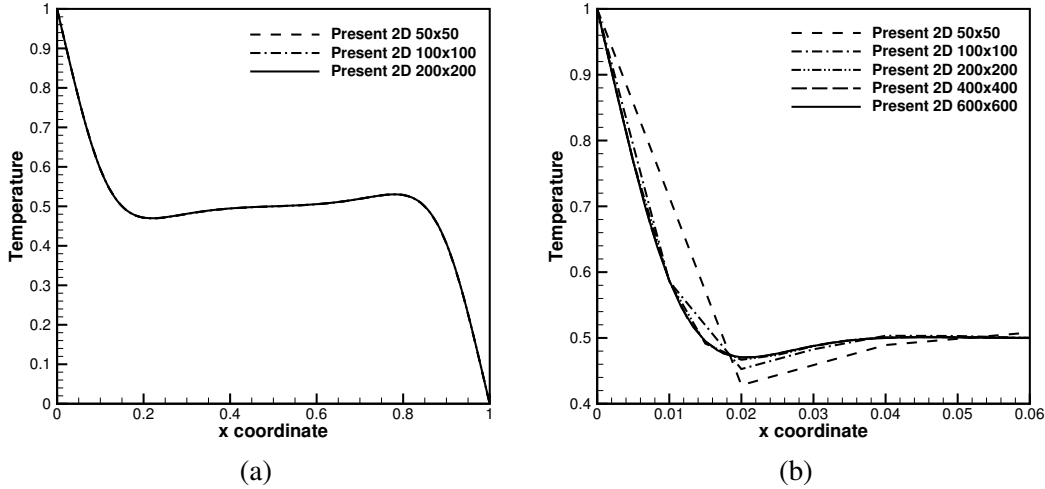


Figure 3: 2D mesh convergence results for mean temperature profile. (a) Laminar case ($Ra = 10^5$). (b) Turbulent case ($Ra = 10^9$).

4.1. 2D cases

4.1.1. Mesh convergence studies

We employ a unit square with a uniform mesh to report consistent results across a range of Ra . The results for 2D cases are shown in Table 1. One can observe that for the laminar cases \overline{Nu} rapidly converges; even a coarse mesh is enough to resolve the thermal boundary layer for these cases. For higher Ra , a denser mesh is required. The convergence of \overline{Nu} value is clear across the wide range of Ra from 10^3 to 10^{10} . We identify the converged value with an underline at each Ra when the difference of \overline{Nu} for two successive mesh densities is less than 2%. The convergence of mean temperature profile is shown in Figure 3.

4.1.2. Comparisons of averaged Nusselt numbers and maximum velocities

To validate the results of our solution, we compare the averaged Nusselt number \overline{Nu} , maximum horizontal velocity along the vertical median line, and maximum vertical velocity along the horizontal median line with previously reported computational results. Note that in what follows,

Table 2: Comparisons of \overline{Nu} and maximum velocities and locations along median lines from $Ra = 10^3$ to $Ra = 10^6$ for the 2D cases.

Ra		Ref. [64]	Ref. [11]	This work
10^3	$U_{\max}(y)$	0.136 (0.813)	0.153 (0.806)	0.138 (0.815)
	$V_{\max}(x)$	0.138 (0.178)	0.155 (0.181)	0.139 (0.180)
	\overline{Nu}	1.118	1.114	1.118
10^4	$U_{\max}(y)$	0.192 (0.823)	0.193 (0.818)	0.194 (0.825)
	$V_{\max}(x)$	0.234 (0.119)	0.234 (0.119)	0.235 (0.120)
	\overline{Nu}	2.243	2.245	2.245
10^5	$U_{\max}(y)$	0.153 (0.855)	0.132 (0.859)	0.132 (0.855)
	$V_{\max}(x)$	0.261 (0.066)	0.258 (0.066)	0.259 (0.065)
	\overline{Nu}	4.519	4.51	4.516
10^6	$U_{\max}(y)$	0.079 (0.850)	0.077 (0.859)	0.078 (0.850)
	$V_{\max}(x)$	0.262 (0.038)	0.260 (0.039)	0.263 (0.040)
	\overline{Nu}	8.799	8.806	8.810

the finest mesh from each convergence study is used when reporting results for the comparisons. We first compare our results with references [11, 64] for the laminar and transition regimes with $Ra \leq 10^6$. These comparisons are shown in Table 2 and illustrate excellent agreement with previous work.

We next compare our results with reference data for the transition and turbulent cases with $Ra \geq 10^7$. Here, we compare our results with reported solutions that were computed using both RANS models [9, 11] and LES models [65, 66] to indicate the difference between them, as shown in Table 3. We see that once Ra goes beyond 10^8 , the RANS models start to produce increasingly diverging results from the more accurate LES models. Our results of \overline{Nu} compare well with the LES models across the complete range of Ra , as expected. We also compare the maximum velocities and corresponding locations in Table 4. Our results compare well with other reported LES results for $Ra = 10^7$ and $Ra = 10^8$. For $Ra = 10^9$, our results generally agree with Dixit and Babu [67] along the horizontal median line, but exhibit a discrepancy for the maximum horizontal velocity. We speculate that this could be due to an under-resolved boundary layer, which may result in different point-wise estimates even though the averaged \overline{Nu} shows converged behavior. We also speculate that when the boundary layer is better resolved, we do not need excessive mesh resolution outside the boundary layers in order to achieve good accuracy of the quantities of interest. To test these speculations, we use a clustered mesh with a mesh density of 100×100 that concentrates elements near all boundaries so that the boundary layer is better resolved. We employ a hyperbolic

Table 3: Comparisons of \overline{Nu} from $Ra = 10^7$ to $Ra = 10^{10}$ for the 2D cases.

Ra	Ref. [9] (RANS)	Ref. [11] (RANS)	Ref. [65] (LES)	Ref. [66] (LES)	This work
10^7	16.47	-	17.2	16.76	16.44
10^8	32.05	32.3	31.2	30.43	30.1
10^9	74.96	60.1	58.1	51.25	54.29
10^{10}	156.85	134.6	-	99.96	97.29

Table 4: Comparisons of the maximum velocities and locations along median lines from $Ra = 10^7$ to $Ra = 10^{10}$ for the 2D cases.

Ra		Ref. [9]	Ref. [67]	Ref. [68]	Ref. [69]	This work
10^7	$U_{\max}(Y)$	-	0.0621 (0.851)	0.0562 (0.879)	0.0548 (0.92)	0.0564 (0.878)
	$V_{\max}(X)$	-	0.265 (0.020)	0.264 (0.021)	0.270 (0.021)	0.264 (0.023)
10^8	$U_{\max}(Y)$	0.0615 (0.941)	0.0466 (0.937)	0.0385 (0.928)	0.0353 (0.94)	0.0399 (0.930)
	$V_{\max}(X)$	0.217 (0.0135)	0.268 (0.0112)	0.266 (0.012)	0.274 (0.013)	0.266 (0.0125)
10^9	$U_{\max}(Y)$	-	0.0190 (0.966)	-	-	0.0270 (0.937)
	$V_{\max}(X)$	-	0.258 (0.0064)	-	-	0.267 (0.00667)
10^{10}	$U_{\max}(Y)$	0.0278 (0.9625)	0.0278 (0.94)	-	-	0.0143 (0.956)
	$V_{\max}(X)$	0.202 (0.0055)	0.257 (0.49)	-	-	0.270 (0.00375)

Table 5: Comparison of the maximum horizontal velocity and the location along the vertical median line for the 2D case of $Ra = 10^9$.

Ra		This work 600 × 600 (uniform)	This work 100 × 100 (stretched)	Ref. [67]
10^9	$U_{\max}(Y)$	0.0270 (0.937)	0.0207 (0.943)	0.0190 (0.966)

tangent stretching function to cluster the uniform mesh. The hyperbolic function is

$$x_{\text{new}} = \frac{1}{2} \left(1 + \frac{\tanh\left(c\left(\frac{x}{L} - \frac{1}{2}\right)\right)}{\tanh\left(\frac{c}{2}\right)} \right), \quad (36)$$

where x is the original coordinate in the uniform mesh, x_{new} is the new coordinate in the stretching direction, L is the domain size in the corresponding stretching direction, and c ($= 5$) is the stretching factor. Table 5 shows the comparison of the maximum horizontal velocity and the location along the vertical median line for $Ra = 10^9$ using uniform and stretched meshes. We can see that the stretched mesh produces results that are closer to the reference data.

4.1.3. Comparisons of mean profiles

We perform comparisons of the mean profiles for a laminar case ($Ra = 10^5$) with Barakos et al. [11] and for a turbulent case ($Ra = 10^9$) with Salat et al. [19]. We report the mean temperature and vertical velocity along the horizontal median line, and the mean temperature and horizontal velocity along the vertical median line, when the data is available in the literature. Figure 4 shows

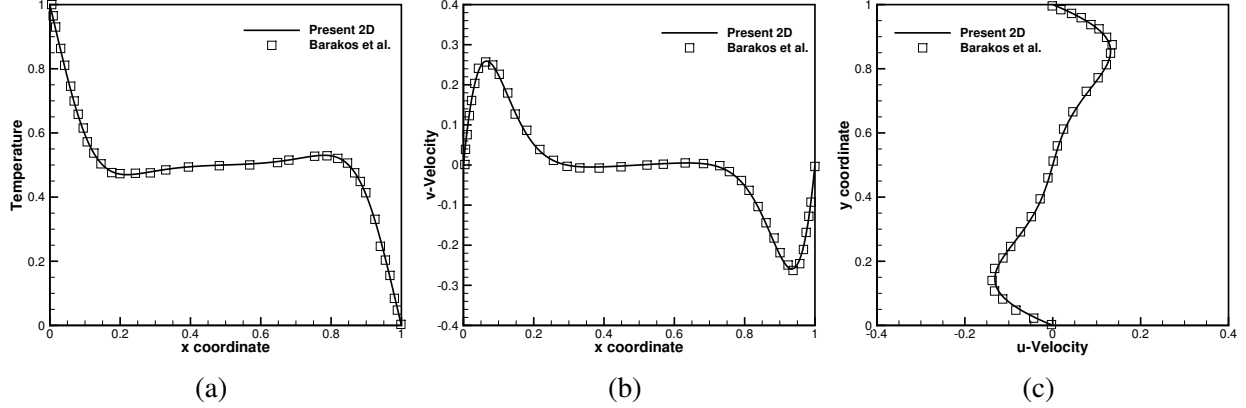


Figure 4: Mean profile comparisons for the present 2D simulation (200×200 uniform mesh) and Barakos et al. [11] at $Ra = 10^5$. (a) The temperature along the horizontal median line. (b) The vertical velocity along the horizontal median line. (c) The horizontal velocity along the vertical median line.

that the simulation results (obtained using a uniform mesh of 200×200) are in excellent agreement with Barakos et al. [11] for the laminar case. For the turbulent case shown in Figure 5, we plot results obtained using both the uniform mesh of 600×600 and the stretched mesh of 100×100 , and compare them to the reference data of Salat et al. [19].³ The comparisons show that the uniform mesh of 600×600 and the stretched mesh of 100×100 produce very similar results that are comparable to the reference results of Salat et al. [19], except for the horizontal velocity along the vertical median line shown in Figure 5d, in which, the stretched mesh of 100×100 produces results that are closer to the reference data. From this study, we conclude that it would be reasonable to deploy this stretched mesh with a similar mesh density in the boundary layer to the 3D cases considered in the next section. In Section 4.3, we will show that imposing the Dirichlet boundary conditions weakly can produce accurate results even on a uniform mesh of 100×100 . We conclude this subsection by plotting 2D contours of temperatures and velocity magnitudes as well as streamlines of the laminar and turbulent cases in Figure 6.

4.2. 3D cases

4.2.1. Mesh convergence studies

We start this subsection by performing mesh convergence studies for two 3D cases: a laminar case with $Ra = 1.89 \times 10^5$ and a turbulent case with $Ra = 1.5 \times 10^9$. The problem setup is shown in Figure 2. To compare with available results from the literature, the laminar case is simulated in a unit cubic cavity, while the turbulent case is simulated in a cuboid with an aspect ratio of $1 \times 1 \times 0.32$, which is identical to the experimental geometry reported in Salat et al. [19]. Uniform meshes are employed for the laminar case. For the turbulent case, we employ the clustered (or

³Note that we compare our results at $Ra = 10^9$ with 2D LES results in Salat et al. [19], which was computed at $Ra = 1.5 \times 10^9$.

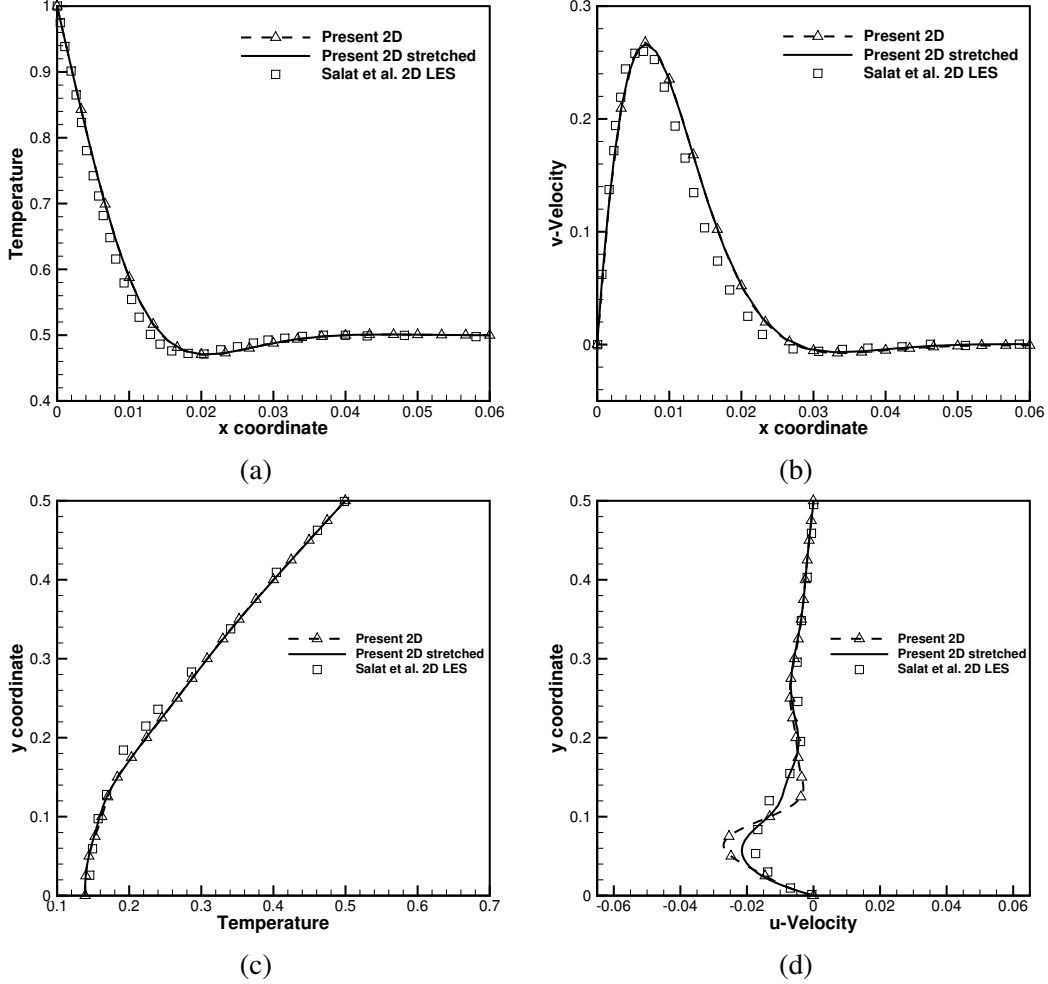


Figure 5: Mean profile comparisons for the present 2D simulations at $Ra = 10^9$ using a 600×600 uniform mesh and a 100×100 stretched mesh, and 2D LES results of Salat et al. [19] at $Ra = 1.5 \times 10^9$. (a) The temperature along the horizontal median line. (b) The vertical velocity along the horizontal median line. (c) The temperature along the vertical median line. (d) The horizontal velocity along the vertical median line.

Table 6: 3D mesh convergence results for \overline{Nu} . The underline indicates the mesh size at which the Nusselt number has reached a converged value. Note that the meshes are uniform for the laminar case of $Ra = 1.89 \times 10^5$ and stretched for the turbulent case of $Ra = 1.5 \times 10^9$.

$Ra = 1.89 \times 10^5$		$Ra = 1.5 \times 10^9$	
$50 \times 50 \times 50$	<u>5.221</u>	$50 \times 50 \times 16$	<u>60.2</u>
$70 \times 70 \times 70$	5.252	$70 \times 70 \times 22$	60.7
$100 \times 100 \times 100$	5.265	$100 \times 100 \times 32$	61.0

stretched) meshes discussed earlier (with $c = 5$). We report convergence results of \overline{Nu} in Table 6. For both cases, the convergence of the surface averaged Nusselt number is rapid. We also show the convergence of mean temperature profile along horizontal median line in Figure 7.

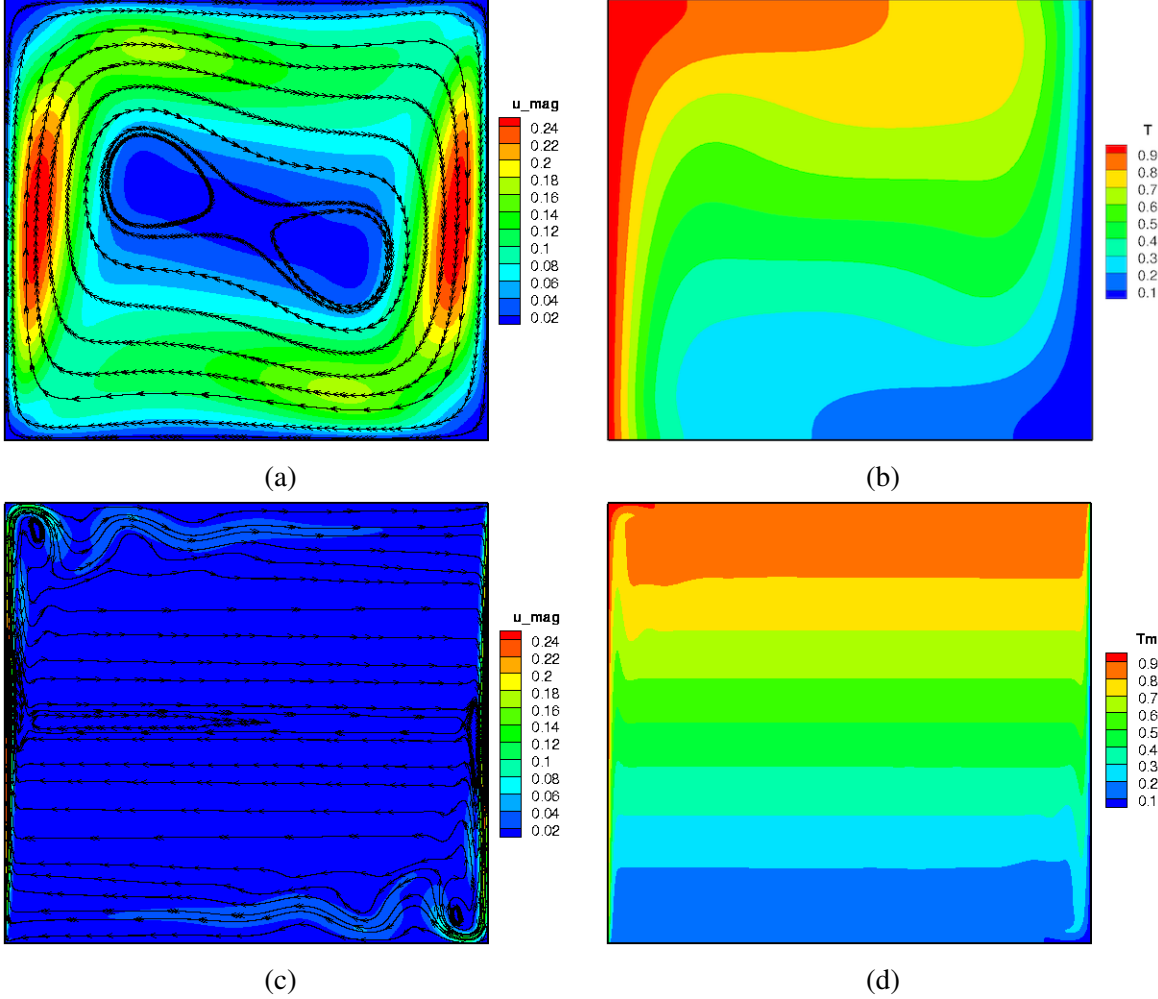


Figure 6: Visualizations of present 2D cases. (a) The streamline and velocity magnitude contour at $Ra = 10^5$. (b) The temperature contour at $Ra = 10^5$. (c) The streamline and velocity magnitude contour at $Ra = 10^9$. (d) The temperature contour at $Ra = 10^9$.

4.2.2. Comparisons of averaged Nusselt numbers

We compare the value of \overline{Nu} for the laminar case using a uniform mesh of $100 \times 100 \times 100$ with available experimental and numerical results in Table 7. Good agreement is observed with the result calculated using a numerical correlation formulation in Fusegi et al. [70] with $Ra = 1.89 \times 10^5$, and the finite-difference simulation results reported in Mallinson and De Vahl Davis [71] with $Ra = 1.5 \times 10^5$. For the turbulent case, we compare the \overline{Nu} obtained using a stretched mesh of $100 \times 100 \times 32$ with the 3D DNS result reported in Salat et al. [19]. This comparison is shown in Table 8 and exhibits good agreement.

4.2.3. Comparisons of mean profiles

We perform mean profile comparisons for the laminar case of $Ra = 1.89 \times 10^5$ with finite-difference simulation results in Fusegi et al. [70] obtained at $Ra = 10^5$ and experimental results

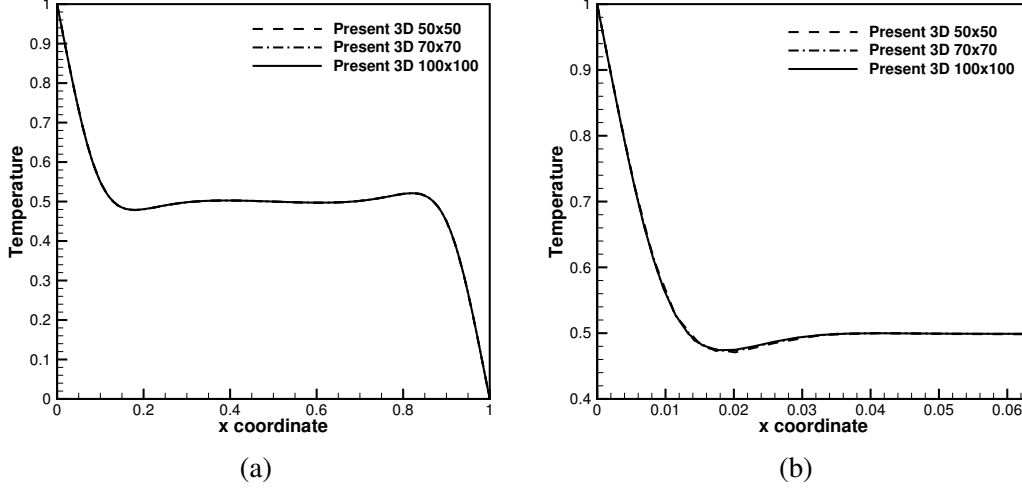


Figure 7: 3D mesh convergence results for mean temperature profile. (a) Laminar case ($Ra = 1.89 \times 10^5$). (b) Turbulent case ($Ra = 1.5 \times 10^9$). Note that the meshes are uniform in the laminar case and stretched in the turbulent case.

Table 7: Comparisons of \overline{Nu} for the 3D laminar case of $Ra = 1.89 \times 10^5$. Note that results in Ref. [71] were obtained at $Ra = 1.5 \times 10^5$.

Ra	This work		Ref. [70]		Ref. [71]	
	Overall	Mid-plane	Overall	Mid-plane	Overall	Mid-plane
1.89×10^5	5.265	5.535	5.252	5.537	5.31	5.71

Table 8: Comparison of \overline{Nu} for the 3D turbulent case of $Ra = 1.5 \times 10^9$. The result in this work is obtained using a stretched mesh of $100 \times 100 \times 32$.

Ra	This work	Ref. [19] (DNS)
1.5×10^9	61.0	60.1

in Krane and Jessee [72] obtained at $Ra = 1.89 \times 10^5$. We plot the mean temperature and vertical velocity along the horizontal median line, and mean temperature and horizontal velocity along the vertical median line, as shown in Figure 8. The overall comparisons are in good agreement as seen in Figures 8a, 8b, and 8d. Along the vertical direction, larger discrepancies are found (between the numerical solutions and experimental result) for the temperature near the top and bottom walls as seen in Figure 8c. Note that both our numerical solution and the numerical solution from Fusegi et al. [70] are in good agreement but differ from the experimental result. This is because it is very difficult to physically maintain a perfect no-heat-flux boundary condition in experiments, which can be clearly seen by the non-perpendicular slope to those walls in the experimental result.⁴

As explained above, it is challenging to maintain a perfect no-heat-flux boundary condition in experiments. Therefore, for the turbulent case of $Ra = 1.5 \times 10^9$, we carry out another simula-

⁴One way to fix this discrepancy is to specify the experimental values of temperature on top and bottom walls as Dirichlet boundary conditions, instead of specifying no-heat-flux boundary conditions.

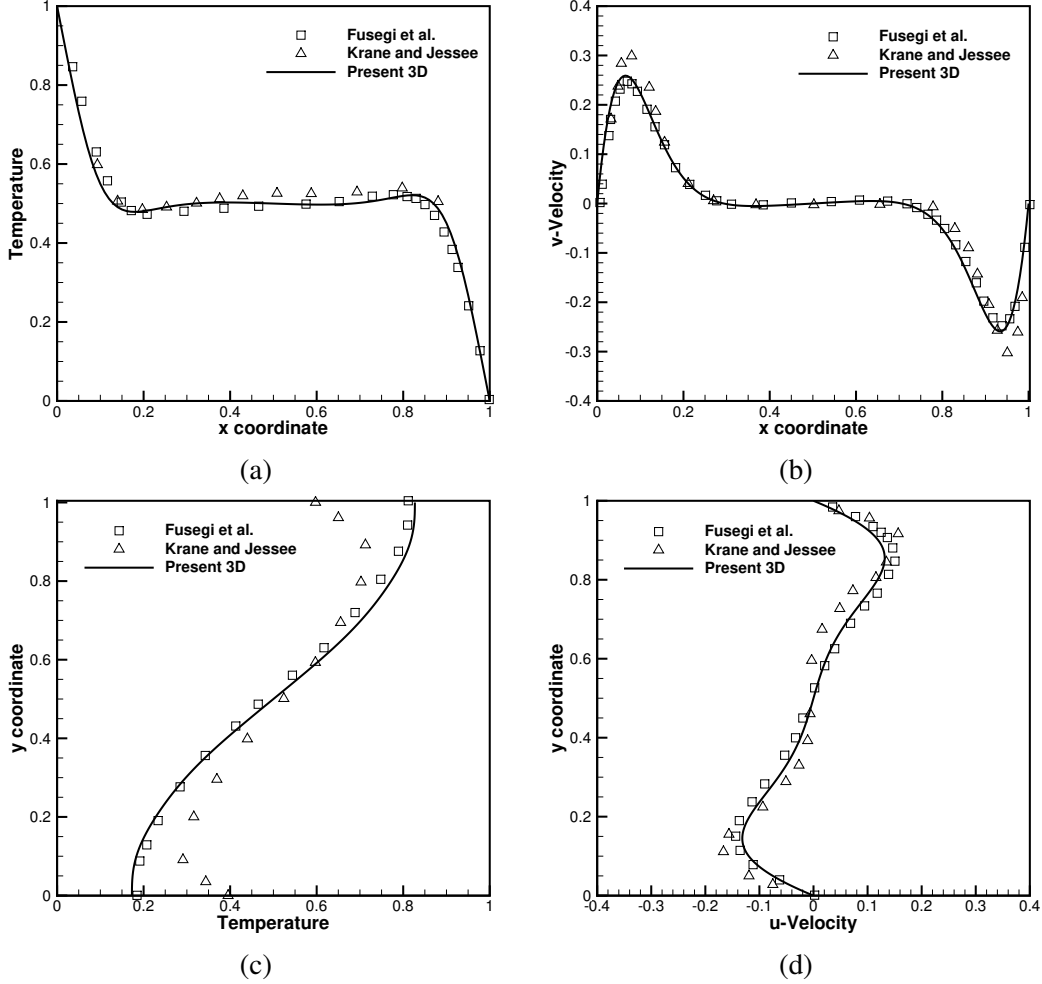


Figure 8: Mean profile comparisons for the present 3D simulation at $Ra = 1.89 \times 10^5$, numerical results of Fusegi et al. [70] at $Ra = 10^5$, and experimental results of Krane and Jessee [72] at $Ra = 1.89 \times 10^5$. (a) The temperature along the horizontal median line. (b) The vertical velocity along the horizontal median line. (c) The temperature along the vertical median line. (d) The horizontal velocity along the vertical median line.

tion (using the same stretched mesh of $100 \times 100 \times 32$) where we impose the experimental values of temperature from Salat et al. [19] at top and bottom walls as Dirichlet boundary conditions, and compare our results with the experimental results, as well as 3D DNS and 3D LES results in Salat et al. [19] using the same Dirichlet boundary conditions. The comparisons are shown in Figure 9. We can see that in the horizontal direction, all the numerical results are nearly identical, but slightly underestimate the temperature compared to the experimental results. For vertical velocity, our 3D result matches the 3D LES result, with minor variations with the 3D DNS results and experimental results. In the vertical direction, all the numerical results are close, but differ from the experimental result for temperature. We speculate that this could again be due to the difficulty in maintaining a constant temperature at these large Ra numbers in the experiment. The horizontal velocity compares very well, with our 3D result matching both the experimental as well as the 3D

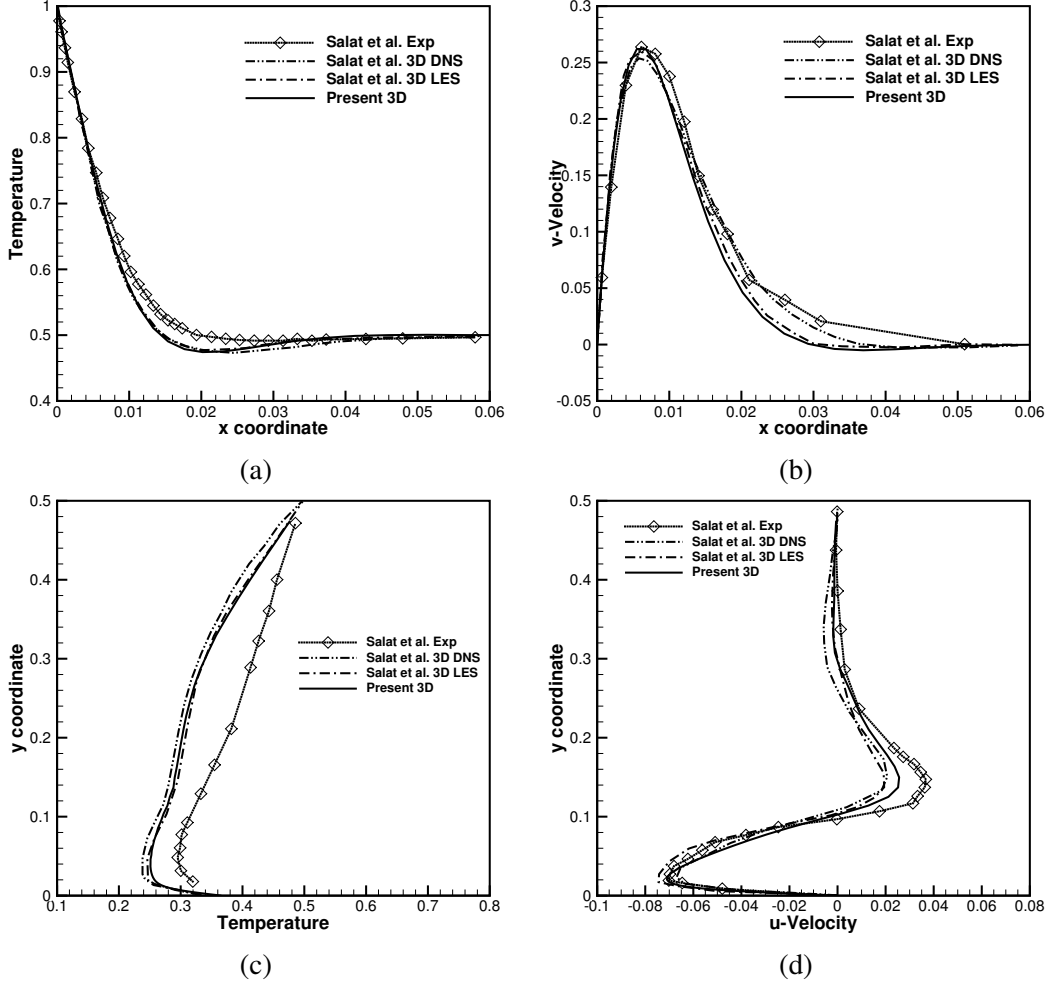


Figure 9: Mean profile comparisons for the present 3D simulation and Salat et al. [19] at $Ra = 1.5 \times 10^9$. (a) The temperature along the horizontal median line. (b) The vertical velocity along the horizontal median line. (c) The temperature along the vertical median line. (d) The horizontal velocity along the vertical median line.

DNS results.

4.2.4. Comparisons of fluctuation profiles for the turbulent case

The comparisons of the fluctuation quantities with Salat et al. [19] for the 3D turbulent case of $Ra = 1.5 \times 10^9$ are shown in Figure 10. Along the horizontal direction, our fluctuation results best match the experimental results for temperature as compared with other numerical results in Figure 10a. The velocity fluctuations are reasonably captured in Figure 10b. Note, however, that the scale of these fluctuations is one order of magnitude bigger than the corresponding fluctuations of the horizontal velocity component in the vertical direction in Figure 10d, which is well captured by our framework. Finally, the temperature fluctuations in the vertical direction are shown in Figure 10c, with all numerical results overestimating the magnitudes. In this case too, the magnitude of the temperature fluctuations is one order magnitude lower than that in the horizontal direction

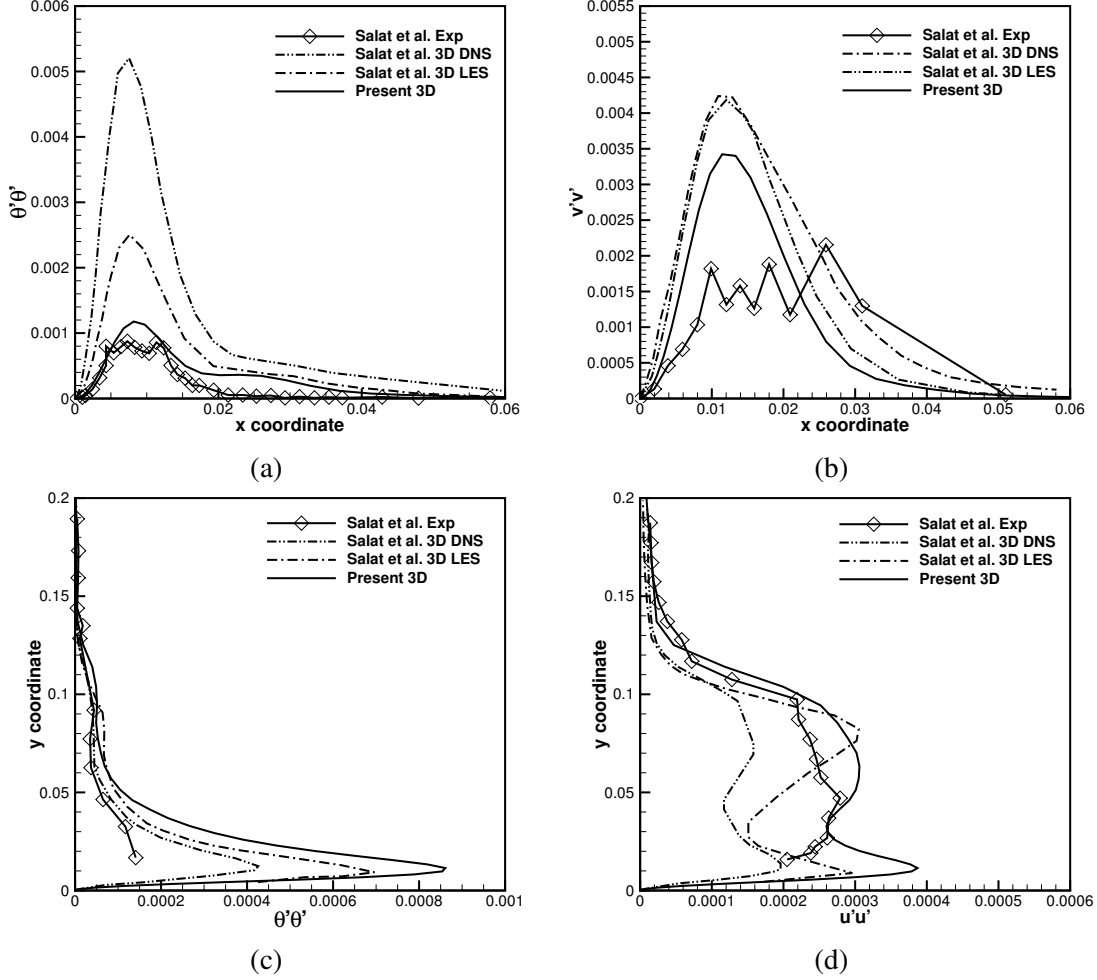


Figure 10: Fluctuation distribution comparisons for the present 3D simulation and Salat et al. [19] at $Ra = 1.5 \times 10^9$. (a) The temperature along horizontal direction. (b) The vertical velocity along horizontal direction. (c) The temperature along vertical direction. (d) The horizontal velocity along vertical direction.

in Figure 10a. Overall, these results suggest that the fluctuations in both temperature and velocity are reasonably well captured by the VMS based approach.

4.3. 2D cases with weakly imposed boundary conditions

4.3.1. Mesh convergence studies

In this subsection, we impose the Dirichlet boundary conditions weakly (termed “weak BC”) using Eq. (31) and re-simulate the 2D cases for Ra from 10^3 to 10^{10} with a uniform mesh. The results are compared to those obtained using strongly imposed Dirichlet boundary conditions (termed “strong BC”) in previous sections. Since the Prandtl number Pr is close to unity, the thickness of the thermal boundary layer will be comparable with that of the fluid boundary layer. As a result, we apply the weak imposition of Dirichlet boundary conditions for both velocity and temperature. Following the conservative traction definition for weak BC of isothermal flows [27], we compute

Table 9: 2D mesh convergence results of \overline{Nu} for weak BC simulations.

Uniform mesh	Ra (Laminar)			Ra (Transition)		Ra (Turbulent)		
	10^3	10^4	10^5	10^6	10^7	10^8	10^9	10^{10}
50×50	<u>1.117</u>	<u>2.241</u>	<u>4.503</u>	<u>8.765</u>	<u>16.35</u>	<u>29.63</u>	61.94	157.1
100×100	1.118	2.244	4.514	8.801	16.44	29.96	<u>53.54</u>	104.3
200×200	1.118	2.245	4.515	8.815	16.48	30.10	54.17	<u>96.08</u>
400×400	-	-	-	-	-	-	54.41	97.46

\overline{Nu} on the hot wall where weak BC is imposed as

$$\overline{Nu} = \frac{\int_{\Gamma_H} \nabla^* \theta \cdot \mathbf{n} \, d\Gamma - \int_{\Gamma_H} \tau_E^{B*} (\theta - \theta_g) \, d\Gamma}{A_H}, \quad (37)$$

where τ_E^{B*} is non-dimensionalized as $\tau_E^{B*} = C_E^B/h^*$, and h^* and θ_g are the non-dimensional wall-normal element size and prescribed Dirichlet temperature at the hot wall, respectively. The mesh convergence results for \overline{Nu} are shown in Table 9. As expected, for the laminar cases, imposing the boundary conditions weakly performs similarly to imposing the boundary conditions strongly (since the strong BC already performed well at coarse meshes). However, for high Ra , weak imposition of Dirichlet boundary conditions shows significant advantages in accurately capturing the thermal boundary effects, even with coarse meshes. For example, the strong BC implementations required a mesh of 400×400 and 600×600 to produce reasonable \overline{Nu} for $Ra = 10^9$ and $Ra = 10^{10}$, respectively, while weak BC only needs a mesh of 100×100 and 200×200 for these cases. These results strongly point to the computational advantages of weak imposition of Dirichlet boundary conditions.

4.3.2. Comparisons with strong BC for the turbulent case

We select a turbulent 2D case with $Ra = 10^9$ and perform detailed comparisons of weakly enforced boundary conditions with a uniform mesh density of 100×100 and strongly enforced boundary conditions with a uniform mesh density of 600×600 . Comparisons of mean profiles along median lines are shown in Figure 11. We first remind the reader that overall good agreement with the reference data [19] was obtained for the strong BC case with a uniform mesh of 600×600 (see Section 4.1.3), except for the horizontal velocity along vertical median line as shown in Figure 5d. Figure 11 shows that good agreement is achieved between the reference data and the results obtained using weakly enforced boundary conditions with a uniform mesh of 100×100 , even for the horizontal velocity (Figure 11d). This was not the case even with a stretched 100×100 mesh using strongly enforced boundary conditions, as demonstrated in Figure 5d.

The maximum horizontal velocities and corresponding vertical locations on median lines for strong BC and weak BC cases are reported in Table 10. One can see that weak imposition of

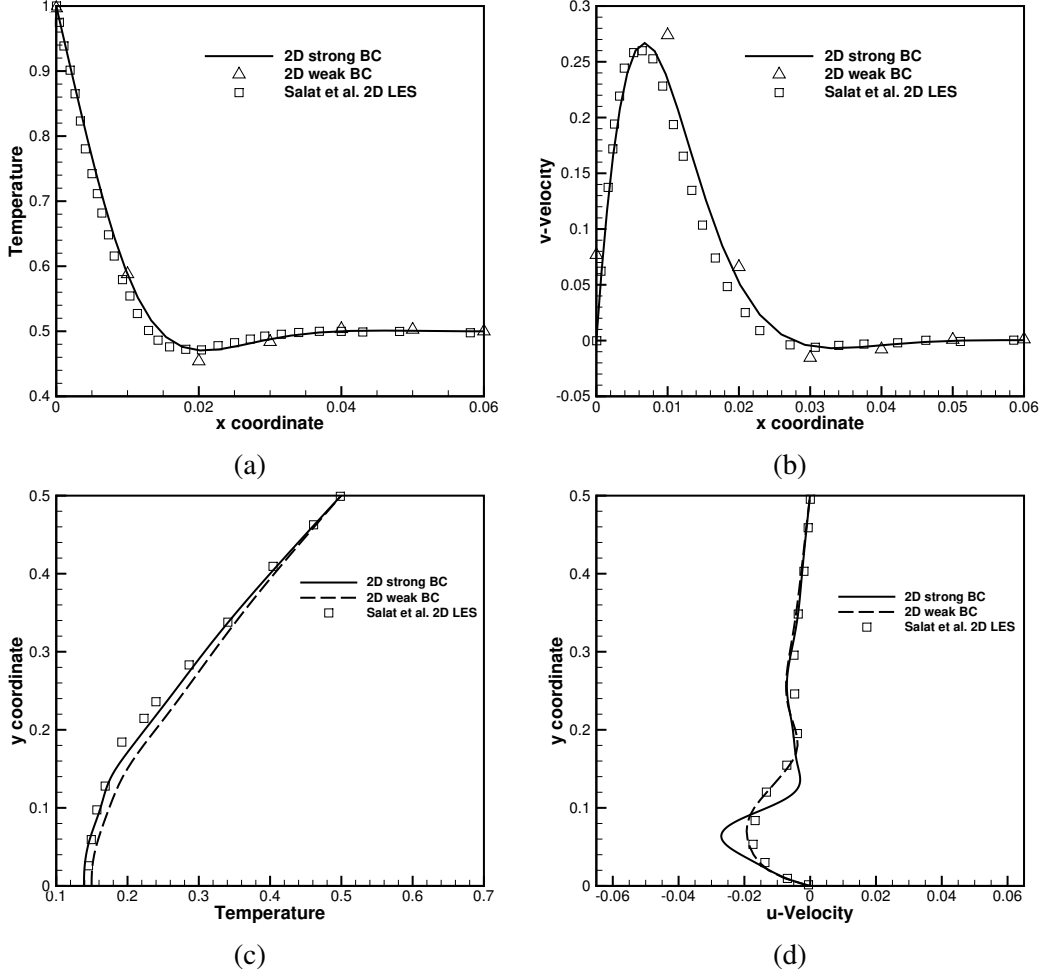


Figure 11: Mean profile comparisons of uniform mesh for 2D strong BC (600×600) and weak BC (100×100) simulations at $Ra = 10^9$. Note that in the horizontal direction, the results are plotted within a thin layer of 0.06 from the hot wall; the weak BC case only has a few data points due to the mesh density. (a) The temperature along the horizontal median line. (b) The vertical velocity along the horizontal median line. (c) The temperature along the vertical median line. (d) The horizontal velocity along the vertical median line.

Table 10: Comparisons of horizontal maximum velocities and locations along vertical median line for 2D strong BC and weak BC simulations at $Ra = 10^9$.

	Strong BC 600×600 (uniform)	Strong BC 100×100 (stretched)	Weak BC 100×100 (uniform)	Ref. [67]
$U_{\max}(Y)$	0.0270 (0.937)	0.0207 (0.943)	0.0191 (0.93)	0.0190 (0.966)

boundary conditions with the mesh density of 100×100 is able to produce accurate results, while imposing the boundary conditions strongly in both uniform mesh of 600×600 and stretched mesh of 100×100 produces less accurate results for this quantity. This result demonstrates the superior coarse-mesh accuracy of weakly enforced boundary conditions.

Table 11: 3D mesh convergence results of \overline{Nu} for weak BC simulations at $Ra = 1.5 \times 10^9$.

Uniform mesh	$Ra = 1.5 \times 10^9$
$50 \times 50 \times 16$	75.2
$70 \times 70 \times 22$	63.3
$100 \times 100 \times 32$	<u>60.1</u>
$150 \times 150 \times 48$	60.8

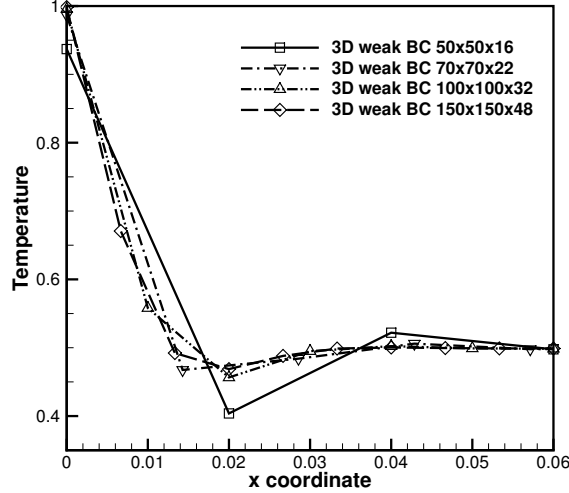


Figure 12: 3D mesh convergence results of the mean temperature profile for weak BC simulations at $Ra = 1.5 \times 10^9$.

4.4. 3D case with weakly imposed boundary conditions

4.4.1. Mesh convergence studies

We further simulate a 3D turbulent case ($Ra = 1.5 \times 10^9$) with weakly enforced Dirichlet boundary conditions to examine the effect of weak BC in 3D simulations. The case setup is exactly the same as in Section 4.2.1 for $Ra = 1.5 \times 10^9$ with the velocity and temperature Dirichlet boundary conditions weakly imposed for uniform mesh densities of $50 \times 50 \times 16$, $70 \times 70 \times 22$, $100 \times 100 \times 32$, $150 \times 150 \times 48$. Note that for all the simulations considered in this section, including the strong BC cases, no-heat-flux boundary conditions are specified at the top and bottom walls. The mesh convergence result for \overline{Nu} along the median line on hot wall is shown in Table 11. The convergence of mean temperature profile along horizontal median line is shown in Figure 12.

4.4.2. Comparisons with strong BC results

To demonstrate the advantage of weak BC in 3D case, we simulate a strong BC case with uniform mesh density of $100 \times 100 \times 32$, and compare the averaged Nusselt number with the weak BC case of the same mesh. Table 12 shows that strong BC with a uniform mesh underestimates \overline{Nu} , while the weak BC produces an accurate result for the same mesh density. The result of the strong BC simulation using stretched mesh from Section 4.2 is also included here for comparison.

Since we have already validated our 3D simulation using stretched mesh with strongly enforced

Table 12: 3D comparison of \overline{Nu} for strong BC (uniform and stretched) and weak BC (uniform) simulations at $Ra = 1.5 \times 10^9$ with mesh density of $100 \times 100 \times 32$.

Ra	Strong BC (uniform)	Strong BC (stretched)	Weak BC (uniform)	Ref. [19] (DNS)
1.5×10^9	46.3	61.0	60.1	60.1

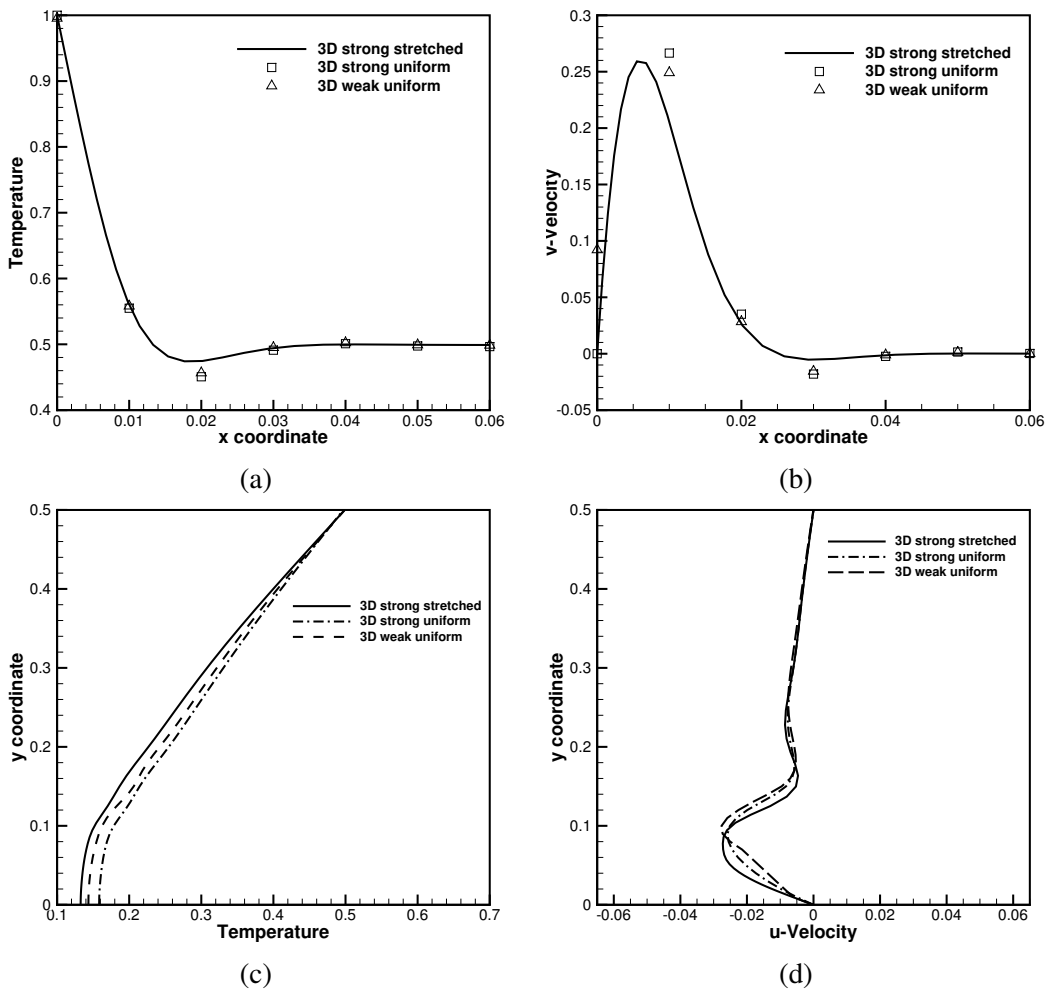


Figure 13: Mean profile comparisons of 3D strong BC (uniform and stretched) and weak BC (uniform) simulations at $Ra = 1.5 \times 10^9$ with same mesh density of $100 \times 100 \times 32$. (a) The temperature along the horizontal median line. (b) The vertical velocity along the horizontal median line. (c) The temperature along the vertical median line. (d) The horizontal velocity along the vertical median line.

boundary conditions in Section 4.2, we use the result as a reference to compare against results of mean profiles simulated using a uniform mesh of $100 \times 100 \times 32$ with both strongly enforced and weakly enforced boundary conditions. Figure 13 shows that for the uniform mesh cases, imposing the boundary conditions weakly produces slightly better results than imposing the boundary conditions strongly. We further emphasize that imposing the boundary conditions weakly produces a more accurate averaged Nusselt number on the hot wall, even with low mesh density. This is

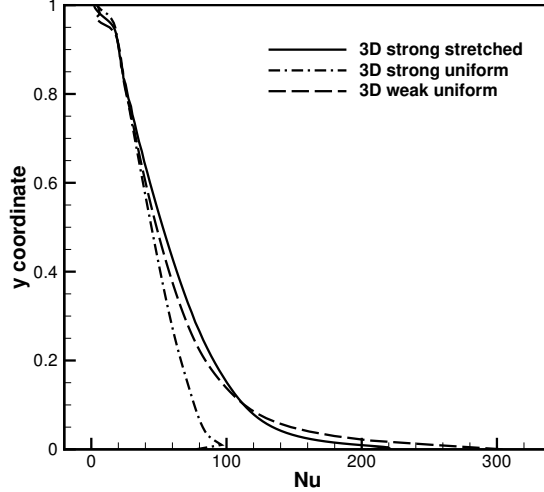


Figure 14: Local Nu along the vertical median line on hot wall at $Ra = 1.5 \times 10^9$ with mesh densities of $100 \times 100 \times 32$ (uniform and stretched).

illustrated in the Nusselt number distribution along the vertical median line on hot wall, as shown in Figure 14, where the weak imposition of the boundary conditions is able to capture the decaying heat transfer coefficient much better than the strongly enforced boundary condition simulation using the same uniform mesh. This is a very promising result and demonstrates the effectiveness of imposing Dirichlet boundary conditions weakly in the context of building energy simulations.

5. Conclusions

We have deployed the variational multiscale method to buoyancy-driven flows, and verified and validated the framework with a Rayleigh–Bénard convection problem for both 2D and 3D cases. We showed excellent comparisons for 2D case across a wide range of Rayleigh numbers, without any special treatments. We also successfully compared simulation results with 3D experimental results as well as other LES and DNS results for both laminar and turbulent conditions. We applied the weak imposition of boundary conditions to the buoyancy-driven flow problem and showed the significant computational advantage of weak imposition of boundary conditions in both 2D and 3D cases. This confirms that the VMS framework with weak imposition of Dirichlet boundary conditions is a computationally efficient approach to model buoyancy-driven flow physics in complex indoor environments. Our future work involves deploying this framework to complex indoor environments to study energy characteristics as well as contaminant transport in the built environment [73, 74].

Acknowledgments

S. Xu, B. Gao and B. Ganapathysubramanian were partially supported by NSF Career Award No. 1149365, and ISU PIIR Award. M.-C. Hsu was partially supported by ARO Grant

No. W911NF-14-1-0296. We thank NSF XSEDE for providing HPC resources that have contributed to the research results reported in this paper.

References

- [1] Office of Energy Efficiency & Renewable Energy (EERE). Buildings Energy Data Book. <https://openei.org/doe-opendata/dataset/buildings-energy-data-book>, 2011. US Department of Energy, Washington, D.C.
- [2] F. Oldewurtel, A. Parisio, C. N. Jones, D. Gyalistras, M. Gwerder, V. Stauch, B. Lehmann, and M. Morari. Use of model predictive control and weather forecasts for energy efficient building climate control. *Energy and Buildings*, 45:15–27, 2012.
- [3] S. Petersen and S. Svendsen. Method for simulating predictive control of building systems operation in the early stages of building design. *Applied Energy*, 88(12):4597–4606, 2011.
- [4] S. Privara, J. Cigler, Z. Váňa, F. Oldewurtel, C. Sagerschnig, and E. Žáčková. Building modeling as a crucial part for building predictive control. *Energy and Buildings*, 56:8–22, 2013.
- [5] S. Privara, J. Široký, L. Ferkl, and J. Cigler. Model predictive control of a building heating system: The first experience. *Energy and Buildings*, 43(2):564–572, 2011.
- [6] C. V. Rao and J. B. Rawlings. Linear programming and model predictive control. *Journal of Process Control*, 10(2):283–289, 2000.
- [7] T. Salsbury, P. Mhaskar, and S. J. Qin. Predictive control methods to improve energy efficiency and reduce demand in buildings. *Computers & Chemical Engineering*, 51:77–85, 2013.
- [8] F. Allard. *Natural Ventilation in Buildings: A Design Handbook*. Earthscan, London, 1998.
- [9] N. C. Markatos and K. A. Pericleous. Laminar and turbulent natural convection in an enclosed cavity. *International Journal of Heat and Mass Transfer*, 27(5):755–772, 1984.
- [10] R. A. W. M. Henkes, F. F. Van Der Vlugt, and C. J. Hoogendoorn. Natural-convection flow in a square cavity calculated with low-Reynolds-number turbulence models. *International Journal of Heat and Mass Transfer*, 34(2):377–388, 1991.
- [11] G. Barakos, E. Mitsoulis, and D. Assimacopoulos. Natural convection flow in a square cavity revisited: Laminar and turbulent models with wall functions. *International Journal for Numerical Methods in Fluids*, 18(7):695–719, 1994.

- [12] A. M. Lankhorst and C. J. Hoogendoorn. Numerical computation of high Rayleigh number natural convection and prediction of hot radiator induced room air motion. *Applied Scientific Research*, 47(4):301–322, 1990.
- [13] K. J. Hsieh and F. S. Lien. Numerical modeling of buoyancy-driven turbulent flows in enclosures. *International Journal of Heat and Fluid Flow*, 25(4):659–670, 2004.
- [14] S. Tieszen, A. Ooi, P. Durbin, and M. Behnia. Modeling of natural convection heat transfer. In *Proceedings of the Summer Program*, pages 287–302, Center for Turbulence Research, Stanford, CA, 1998.
- [15] M. Santamouris and F. Allard. *Natural Ventilation in Buildings: A Design Handbook*. Earthscan, London, 1998.
- [16] Z. Zhai. Application of computational fluid dynamics in building design: Aspects and trends. *Indoor and Built Environment*, 15(4):305–313, 2006.
- [17] Y. Li and P. V. Nielsen. CFD and ventilation research. *Indoor Air*, 21(6):442–453, 2011.
- [18] D. Etheridge. A perspective on fifty years of natural ventilation research. *Building and Environment*, 91:51–60, 2015.
- [19] J. Salat, S. Xin, P. Joubert, A. Sergent, F. Penot, and P. Le Quéré. Experimental and numerical investigation of turbulent natural convection in a large air-filled cavity. *International Journal of Heat and Fluid Flow*, 25(5):824–832, 2004.
- [20] S.-H. Peng and L. Davidson. Large eddy simulation for turbulent buoyant flow in a confined cavity. *International Journal of Heat and Fluid Flow*, 22(3):323–331, 2001.
- [21] A. Sergent, P. Joubert, and P. Le Quéré. Development of a local subgrid diffusivity model for large-eddy simulation of buoyancy-driven flows: Application to a square differentially heated cavity. *Numerical Heat Transfer: Part A: Applications*, 44(8):789–810, 2003.
- [22] C. Van Treeck, E. Rank, M. Krafczyk, J. Tölke, and B. Nachtwey. Extension of a hybrid thermal LBE scheme for large-eddy simulations of turbulent convective flows. *Computers & Fluids*, 35(8):863–871, 2006.
- [23] T. J. R. Hughes, L. Mazzei, and K. E. Jansen. Large eddy simulation and the variational multiscale method. *Computing and Visualization in Science*, 3:47–59, 2000.

- [24] T. J. R. Hughes, L. Mazzei, A. A. Oberai, and A. Wray. The multiscale formulation of large eddy simulation: Decay of homogeneous isotropic turbulence. *Physics of Fluids*, 13: 505–512, 2001.
- [25] Y. Bazilevs, V. M. Calo, J. A. Cottrell, T. J. R. Hughes, A. Reali, and G. Scovazzi. Variational multiscale residual-based turbulence modeling for large eddy simulation of incompressible flows. *Computer Methods in Applied Mechanics and Engineering*, 197(1):173–201, 2007.
- [26] K. Takizawa, T. E. Tezduyar, and T. Kuraishi. Multiscale space–time methods for thermo-fluid analysis of a ground vehicle and its tires. *Mathematical Models and Methods in Applied Sciences*, 25(12):2227–2255, 2015.
- [27] Y. Bazilevs and I. Akkerman. Large eddy simulation of turbulent Taylor–Couette flow using isogeometric analysis and the residual-based variational multiscale method. *Journal of Computational Physics*, 229(9):3402–3414, 2010.
- [28] J. Yan, A. Korobenko, A. E. Tejada-Martínez, R. Golshan, and Y. Bazilevs. A new variational multiscale formulation for stratified incompressible turbulent flows. *Computers & Fluids*, 158:150–156, 2017.
- [29] Y. Bazilevs, A. Korobenko, J. Yan, A. Pal, S. M. I. Gohari, and S. Sarkar. ALE–VMS formulation for stratified turbulent incompressible flows with applications. *Mathematical Models and Methods in Applied Sciences*, 25(12):2349–2375, 2015.
- [30] M.-C. Hsu, I. Akkerman, and Y. Bazilevs. Finite element simulation of wind turbine aerodynamics: validation study using NREL Phase VI experiment. *Wind Energy*, 17(3):461–481, 2014.
- [31] Y. Bazilevs, K. Takizawa, T. E. Tezduyar, M.-C. Hsu, N. Kostov, and S. McIntyre. Aerodynamic and FSI analysis of wind turbines with the ALE–VMS and ST–VMS methods. *Archives of Computational Methods in Engineering*, 21:359–398, 2014.
- [32] K. Takizawa, Y. Bazilevs, T. E. Tezduyar, M.-C. Hsu, O. Øiseth, K. M. Mathisen, N. Kostov, and S. McIntyre. Engineering analysis and design with ALE–VMS and Space–Time methods. *Archives of Computational Methods in Engineering*, 21:481–508, 2014.
- [33] K. Takizawa, Y. Bazilevs, T. E. Tezduyar, C. C. Long, A. L. Marsden, and K. Schjodt. ST and ALE–VMS methods for patient-specific cardiovascular fluid mechanics modeling. *Mathematical Models and Methods in Applied Sciences*, 24:2437–2486, 2014.

- [34] C. Wang, M. C. H. Wu, F. Xu, M.-C. Hsu, and Y. Bazilevs. Modeling of a hydraulic arresting gear using fluid–structure interaction and isogeometric analysis. *Computers & Fluids*, 142: 3–14, 2017.
- [35] J. Yan, S. Lin, Y. Bazilevs, and G. J. Wagner. Isogeometric analysis of multi-phase flows with surface tension and with application to dynamics of rising bubbles. *Computers & Fluids*, 2018.
- [36] D. Sondak, J. N. Shadid, A. A. Oberai, R. P. Pawlowski, E. C. Cyr, and T. M. Smith. A new class of finite element variational multiscale turbulence models for incompressible magneto-hydrodynamics. *Journal of Computational Physics*, 295:596–616, 2015.
- [37] J. Liu and A. A. Oberai. The residual-based variational multiscale formulation for the large eddy simulation of compressible flows. *Computer Methods in Applied Mechanics and Engineering*, 245:176–193, 2012.
- [38] Y. Bazilevs and T. J. R. Hughes. Weak imposition of Dirichlet boundary conditions in fluid mechanics. *Computers & Fluids*, 36:12–26, 2007.
- [39] Y. Bazilevs, C. Michler, V. M. Calo, and T. J. R. Hughes. Isogeometric variational multiscale modeling of wall-bounded turbulent flows with weakly enforced boundary conditions on unstretched meshes. *Computer Methods in Applied Mechanics and Engineering*, 199:780–790, 2010.
- [40] M.-C. Hsu, I. Akkerman, and Y. Bazilevs. Wind turbine aerodynamics using ALE–VMS: Validation and the role of weakly enforced boundary conditions. *Computational Mechanics*, 50(4):499–511, 2012.
- [41] Y. Bazilevs, C. Michler, V. M. Calo, and T. J. R. Hughes. Weak Dirichlet boundary conditions for wall-bounded turbulent flows. *Computer Methods in Applied Mechanics and Engineering*, 196(49):4853–4862, 2007.
- [42] K. Takizawa, T. E. Tezduyar, T. Kuraishi, S. Tabata, and H. Takagi. Computational thermo-fluid analysis of a disk brake. *Computational Mechanics*, 57(6):965–977, 2016.
- [43] A. Korobenko, J. Yan, S. M. I. Gohari, S. Sarkar, and Y. Bazilevs. FSI simulation of two back-to-back wind turbines in atmospheric boundary layer flow. *Computers & Fluids*, 158: 167–175, 2017.
- [44] C. Johnson. *Numerical Solution of Partial Differential Equations by the Finite Element Method*. Cambridge University Press, Sweden, 1987.

- [45] S. C. Brenner and L. R. Scott. *The Mathematical Theory of Finite Element Methods, 2nd ed.* Springer, Berlin, 2002.
- [46] Y. Bazilevs, K. Takizawa, and T. E. Tezduyar. *Computational Fluid–Structure Interaction: Methods and Applications.* John Wiley & Sons, Chichester, 2013.
- [47] A. N. Brooks and T. J. R. Hughes. Streamline upwind/Petrov–Galerkin formulations for convection dominated flows with particular emphasis on the incompressible Navier–Stokes equations. *Computer Methods in Applied Mechanics and Engineering*, 32:199–259, 1982.
- [48] T. E. Tezduyar, S. Mittal, S. E. Ray, and R. Shih. Incompressible flow computations with stabilized bilinear and linear equal-order-interpolation velocity-pressure elements. *Computer Methods in Applied Mechanics and Engineering*, 95(2):221–242, 1992.
- [49] J. Nitsche. Über ein Variationsprinzip zur Lösung von Dirichlet-Problemen bei Verwendung von Teilräumen, die keinen Randbedingungen unterworfen sind. *Abhandlungen aus dem Mathematischen Seminar der Universität Hamburg*, 36:9–15, 1971.
- [50] R. Golshan, A. E. Tejada-Martínez, M. Juha, and Y. Bazilevs. Large-eddy simulation with near-wall modeling using weakly enforced no-slip boundary conditions. *Computers & Fluids*, 118:172–181, 2015.
- [51] F. Xu, G. Moutsanidis, D. Kamensky, M.-C. Hsu, M. Murugan, A. Ghoshal, and Y. Bazilevs. Compressible flows on moving domains: Stabilized methods, weakly enforced essential boundary conditions, sliding interfaces, and application to gas-turbine modeling. *Computers & Fluids*, 158:201–220, 2017.
- [52] T. Kanai, K. Takizawa, T. E. Tezduyar, T. Tanaka, and A. Hartmann. Compressible-flow geometric-porosity modeling and spacecraft parachute computation with isogeometric discretization. *Computational Mechanics*, 63:301–321, 2018.
- [53] D. Kamensky, M.-C. Hsu, D. Schillinger, J. A. Evans, A. Aggarwal, Y. Bazilevs, M. S. Sacks, and T. J. R. Hughes. An immersogeometric variational framework for fluid–structure interaction: Application to bioprosthetic heart valves. *Computer Methods in Applied Mechanics and Engineering*, 284:1005–1053, 2015.
- [54] F. Xu, D. Schillinger, D. Kamensky, V. Varduhn, C. Wang, and M.-C. Hsu. The tetrahedral finite cell method for fluids: Immersogeometric analysis of turbulent flow around complex geometries. *Computers & Fluids*, 141:135–154, 2016.

- [55] M.-C. Hsu, C. Wang, F. Xu, A. J. Herrema, and A. Krishnamurthy. Direct immersogeometric fluid flow analysis using B-rep CAD models. *Computer Aided Geometric Design*, 43:143–158, 2016.
- [56] C. Wang, F. Xu, M.-C. Hsu, and A. Krishnamurthy. Rapid B-rep model preprocessing for immersogeometric analysis using analytic surfaces. *Computer Aided Geometric Design*, 52–53:190–204, 2017.
- [57] F. Xu, Y. Bazilevs, and M.-C. Hsu. Immersogeometric analysis of compressible flows with application to aerodynamic simulation of rotorcraft. *Mathematical Models and Methods in Applied Sciences*, 2019. <https://doi.org/10.1142/S0218202519410033>.
- [58] D. N. Arnold, F. Brezzi, B. Cockburn, and L. D. Marini. Unified analysis of discontinuous Galerkin methods for elliptic problems. *SIAM Journal of Numerical Analysis*, 39:1749–1779, 2002.
- [59] M. Juntunen and R. Stenberg. Nitsche’s method for general boundary conditions. *Mathematics of Computation*, 78(267):1353–1374, 2009.
- [60] A. Embar, J. Dolbow, and I. Harari. Imposing Dirichlet boundary conditions with Nitsche’s method and spline-based finite elements. *International Journal for Numerical Methods in Engineering*, 83(7):877–898, 2010.
- [61] T. E. Tezduyar, S. Sathe, R. Keedy, and K. Stein. Space–time finite element techniques for computation of fluid–structure interactions. *Computer Methods in Applied Mechanics and Engineering*, 195:2002–2027, 2006.
- [62] S. Balay, S. Abhyankar, M. F. Adams, J. Brown, P. Brune, K. Buschelman, L. Dalcin, A. Dener, V. Eijkhout, W. D. Gropp, D. Kaushik, M. G. Knepley, D. A. May, L. C. McInnes, R. T. Mills, T. Munson, K. Rupp, P. Sanan, B. F. Smith, S. Zampini, H. Zhang, and H. Zhang. PETSc users manual. Technical Report ANL-95/11 - Revision 3.10, Argonne National Laboratory, 2018. <http://www.mcs.anl.gov/petsc>.
- [63] K. Schloegel, G. Karypis, and V. Kumar. ParMETIS - Parallel Graph Partitioning and Fill-reducing Matrix Ordering , Version 4.0.3. <http://glaros.dtc.umn.edu/gkhome/metis/parmetis/overview>, 2013. University of Minnesota, Minneapolis, MN.
- [64] G. De Vahl Davis. Natural convection of air in a square cavity: A bench mark numerical solution. *International Journal for Numerical Methods in Fluids*, 3(3):249–264, 1983.

- [65] H. Sajjadi, M. Gorji, S. F. Hosseinizadeh, G. R. Kefayati, and D. D. Ganji. Numerical analysis of turbulent natural convection in square cavity using large-eddy simulation in lattice Boltzmann method. *Iranian Journal of Science and Technology, Transactions of Mechanical Engineering*, 35(M2):133, 2011.
- [66] S. Chen, H. Liu, and C. Zheng. Numerical study of turbulent double-diffusive natural convection in a square cavity by LES-based lattice Boltzmann model. *International Journal of Heat and Mass Transfer*, 55(17):4862–4870, 2012.
- [67] H. N. Dixit and V. Babu. Simulation of high Rayleigh number natural convection in a square cavity using the lattice Boltzmann method. *International Journal of Heat and Mass Transfer*, 49(3):727–739, 2006.
- [68] P. Le Quéré. Accurate solutions to the square thermally driven cavity at high Rayleigh number. *Computers & Fluids*, 20(1):29–41, 1991.
- [69] D. C. Wan, B. S. V. Patnaik, and G. W. Wei. A new benchmark quality solution for the buoyancy-driven cavity by discrete singular convolution. *Numerical Heat Transfer: Part B: Fundamentals*, 40(3):199–228, 2001.
- [70] T. Fusegi, J. M. Hyun, K. Kuwahara, and B. Farouk. A numerical study of three-dimensional natural convection in a differentially heated cubical enclosure. *International Journal of Heat and Mass Transfer*, 34(6):1543–1557, 1991.
- [71] G. D. Mallinson and G. De Vahl Davis. Three-dimensional natural convection in a box: A numerical study. *Journal of Fluid Mechanics*, 83(1):1–31, 1977.
- [72] R. J. Krane and J. Jessee. Some detailed field measurements for a natural convection flow in a vertical square enclosure. In *Proceedings of the First ASME-JSME Thermal Engineering Joint Conference*, volume 1, pages 323–329, 1983.
- [73] A. Fontanini, M. G. Olsen, and B. Ganapathysubramanian. Thermal comparison between ceiling diffusers and fabric ductwork diffusers for green buildings. *Energy and Buildings*, 43(11):2973–2987, 2011.
- [74] A. Fontanini, U. Vaidya, and B. Ganapathysubramanian. A methodology for optimal placement of sensors in enclosed environments: A dynamical systems approach. *Building and Environment*, 100:145–161, 2016.